Bachelor Thesis at the LMU Munich

Bachelorarbeit an der LMU München

Calibration of a Photometric Filter System with a 5-inch Telescope Subsystem of the MAGIC Telescopes

Kalibrierung eines photometrischen Filtersystems mit einem 5-Zoll-Teleskopsubsystem der MAGIC-Teleskope

Marine Pihet

Max-Planck-Institute for Physics

Max-Planck-Institut für Physik

December 16, 2020

supervised by Prof. Dr. Thomas Kuhr

Abstract

In this Bachelor thesis, the photometric calibration of the 5-inch MAGIC Atmosphere Minion (MAM) telescope on the Canary Island of La Palma, Spain, is presented. The telescope is supposed to measure the atmospheric transmission in real time and in pointing direction of the Major Atmospheric Gamma-Ray Imaging Cherenkov (MAGIC) telescopes, also situated on La Palma. Different concepts of photometry are discussed and their suitability is evaluated according to the special observing conditions in which MAM will be operating. These include possibly challenging weather conditions, very large zenith angle observations, and an automatic mode of operation.

The task of MAM is motivated by the need to correct MAGIC data for the effect of atmospheric extinction. When a gamma ray enters Earth's atmosphere it produces an electromagnetic air shower of secondary particles, which can be observed by MAGIC because of the Cherenkov radiation they emit. Knowledge about the amount of Cherenkov light surviving the way through the atmosphere is crucial for the correct reconstruction of the primary gamma-ray energy. MAM is equipped with two telescope tubes, a spectrograph, and several cameras for imaging. Only the 5-inch telescope and a CMOS camera were used for this Bachelor work. The calibration measurement was done remotely during good weather conditions. Five stars with a wide range of color indices were observed in the l, r, g, and b filter from the Baader company and at different zenith angles ranging from $28\,^\circ$ to $80\,^\circ$. Existing software and some modules, especially written for the purpose of this thesis, were used for the control of the telescope. From the data, extinction coefficients in different bands of the visible spectrum at the site of the Roque de los Muchachos observatory were calculated and compared to other measurements. They were found to match the expectation and agree with the dependency on wavelength and color of the observed star. As a final result, color transformation relations between the Landolt photometric standard system and the MAM observational system were derived for the filters r, g and b. The results for filter r are found to be inconsistent and an attempt is made to explain this. Results for filter g and b are consistent and stable, but precision should be improved to enable more concrete statements. The main conclusion is that more stars are needed to reliably characterise the transformation relations and reduce uncertainties.

A reevaluation of the photometric concepts shows that the concept based on an existing catalog of stars has potential for success, but is more complex and susceptible for systematic uncertainties arising from the transformation between photometric systems. The concept based on the MAM observational system is simpler and can give quicker first results with less effort.

Contents

Acronyms

AM	Airmass
ARCADE	Atmospheric Research for Climate and Astroparticle DEtection
AGN	Active Galactic Nuclei
CCD	Charged Coupled Device
CMOS	Complementary Metal-Oxide Semiconductor
CTA	Cherenkov Telescope Array
FITS	Flexible Image Transport System
FoV	Field of View
FRAM	F/(Ph)otometric Robotic Atmospheric Monitor
GRB	Gamma-Ray Burst
IACT	Imaging Atmospheric Cherenkov Telescope
LIDAR	LIght Detection And Ranging system
MAGIC	Major Atmospheric Gamma-Ray Imaging Cherenkov Telescopes
MAM	MAGIC Atmosphere Minion
ORM	Observatorio del Roque de los Muchachos
PMT	Photomultiplier Tube
PSF	Point Spread Function
RMS	Root Mean Square
SNR	Signal-to-Noise Ratio
(V)AOD	(Vertical) Aerosol Optical Depth
VHE	Very High Energy
VLZA	Very Large Zenith Angle

List of Figures

List of Tables

1 Introduction

The following two sections will give a brief introduction to gamma-ray astrophysics, to the MAGIC telescopes, and to the role of atmospheric monitoring and calibration subsystems in MAGIC, providing additional data for the analysis.

1.1 Very high energy gamma-ray astronomy

Very High Energy (VHE) gamma-ray physics is a term describing a branch of astrophysics, which observes and studies the high energy part of the electromagnetic spectrum originating from different astrophysical sources. The main targets of observation are very high energy photons, or gamma rays. VHE gamma rays are produced in the most extreme conditions that exist in the Universe. Sources emitting them can be galactic, like supernova remnants and pulsars, or extragalactic, like Active Galactic Nuclei (AGN) and Gamma-Ray Bursts (GRBs)[1]. AGN are the center regions of galaxies containing an active supermassive black hole and an accretion disk of material around it. The disk produces extremely luminous electromagnetic radiation, which is mainly emitted along two jets emerging perpendicular to the plane of the disk. AGN are often far away sources (100's of millions to billions of light years away), but can be detected because they are very bright. AGN are classified into different subcategories depending on spectral and orientational properties. For instance, if the jet points directly to Earth, the AGN is called a blazar.

When a gamma ray arrives at Earth it enters the atmosphere and produces an air shower of secondary particles. Photons produce especially narrow air showers, because the electromagnetic processes in the shower do not generate a lot of transverse momentum. Processes involved are the pair production of electron-positron pairs and emission of bremsstrahlung by the electrons and positrons. The particles emit another kind of radiation at the same time because their velocity exceeds the speed of light in the atmosphere. This process is known as Cherenkov effect and the emitted Cherenkov radiation mostly lies in the blue and ultraviolet part of the spectrum. The sum of Cherenkov light from all the shower particles is emitted inside a cone of a certain opening angle ($\lesssim 1\,°$). This angle depends on the refractive index of air. The diameter of the cone grows as it travels through the atmosphere and produces a lightpool when it reaches the ground. If a telescope happens to be inside of the light pool it can detect the Cherenkov light. There are other particles capable of producing air showers, like protons. Actually most of the air showers are produced by protons because they are a lot more abundant than the rare VHE gamma rays, even when pointing to a strong gamma-ray source [11].

Figure 1 illustrates a photon-induced electromagnetic and a proton-induced hadronic

[1] GRBs are very short-lived sudden outbursts of gamma-ray emission. The nature of this process is not well understood to this date.

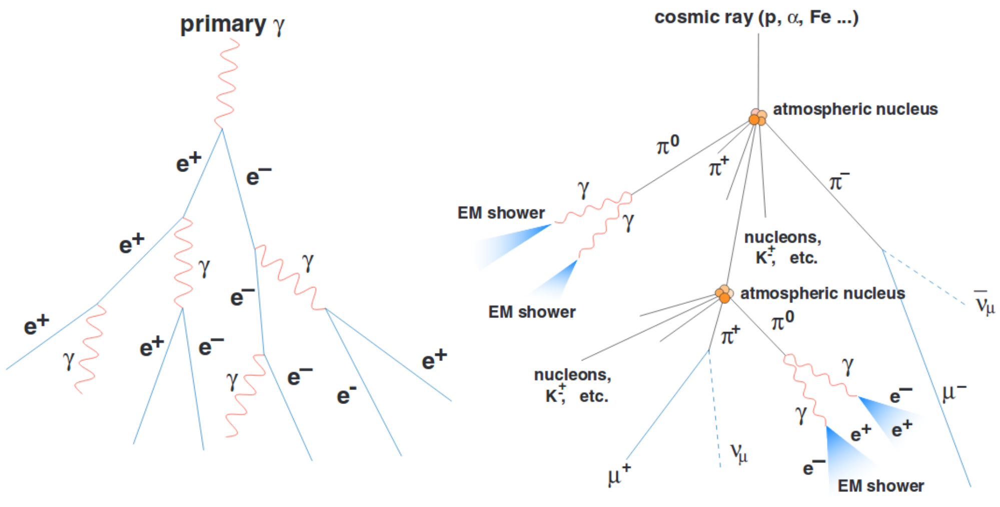

Figure 1: Particle air showers in the atmosphere. Left: Electromagnetic shower produced by a photon. Right: Hadronic shower produced by a proton or other nucleus. Protons produce showers that are more scattered in the lateral direction due to the numerous subshowers (e. g., electromagnetic (EM) subshowers). Proton showers consist of many different secondary particles, e. g., nuclei, pions, kaons, electrons/positrons, nucleons and neutrinos. Image taken from [43].

shower.

1.2 MAGIC and very large zenith angle observations

The MAGIC telescopes are two 17 m Imaging Atmospheric Cherenkov Telescopes (IACTs) on the Canary Island of La Palma, Spain. MAGIC stands for Major Atmospheric Gamma-Ray Imaging Cherenkov Telescope. Such earth-bound telescopes detect the Cherenkov radiation from the secondary particles of an air shower using an array of photomultiplier tubes (PMTs) as a camera. They use the atmosphere as a calorimeter to reconstruct the energy of the primary gamma ray that hit the atmosphere and produced the shower. For correct conclusions, proper reduction and cleaning routines have to be applied to the data. The operation and data analysis require additional data from atmospheric monitors or calibration subsystems. Three of these will be mentioned below:

1. The allsky camera of MAGIC is installed on the roof of the MAGIC counting house, which can be seen in Figure 2. During an observation, the operators of the telescopes can use it to monitor the sky and potential clouds. However, the

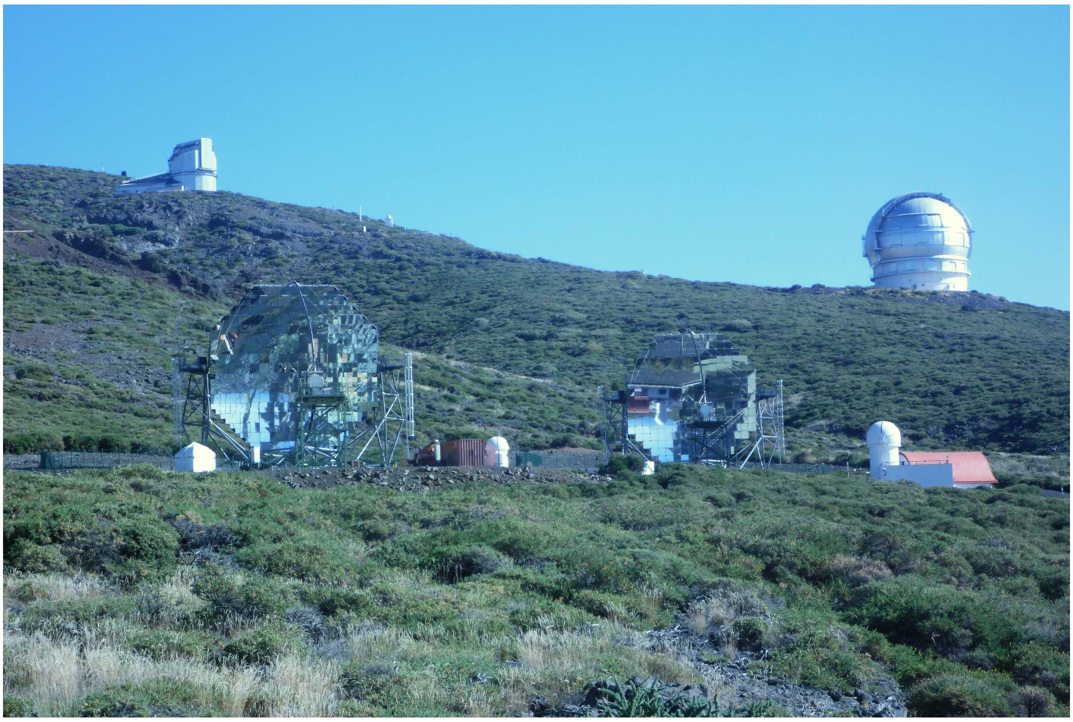

Figure 2: The MAGIC telescopes at the Roque de los Muchachos Observatory (ORM) in La Palma, Spain. MAGIC 1 is on the left, MAGIC 2 on the right side of the image. The small building to the right of MAGIC 2 is the counting house. From there the MAGIC telescopes are operated during the night. The white dome on the counting house contains the LIDAR system. To the left of MAGIC 1 the FRAM telescope can be seen, which is also an instrument for atmospheric monitoring (will be mentioned again later). Between the gamma-ray telescopes there is another small white dome containing the optical subsystem MAM used for this Bachelor thesis. In the background two more of the telescopes at ORM can be seen.

camera can not detect all clouds, especially thin layers will not be visible[2]. This is mentioned here because during the observations for this Bachelor thesis, the allsky camera was used in a similar way.

2. Another subsystem is the Light Detection and Ranging system (LIDAR) [10], which is located inside the dome on the counting house. It is a 60 cm reflector telescope with a laser attached on one side. By shooting the laser into the atmosphere and measuring the backscatter on aerosols and air molecules, it can determine the atmospheric transmission in pointing direction of MAGIC. Only a part of the Cherenkov light produced by an air shower reaches the detector of MAGIC because of absorption and scattering processes in the atmosphere. This leads to an

[2]There are attempts to automatize the detection of clouds on allsky cameras [1].

underestimation of the primary gamma-ray energy. Transmission data from the LIDAR can be used to correct this energy upwards.

3. Data for this Bachelor work was taken with the MAGIC Atmosphere Minion (MAM) subsystem of MAGIC. It is located inside of the fenced area of MAGIC 1 and can also be seen in Figure 2, between the two MAGIC telescopes, to the right of the red container. More details about this subsystem will be described in the next chapter.

There is a special mode of operation called Very Large Zenith Angle (VLZA) observations used in MAGIC [31]. The zenith angle of a target is the angle between the zenith point and the target (definition of the zenith angle in section 3.2.1). MAGIC purposefully observes targets at very large zenith angles during these observations. This is not typical because along with the high zenith angle several difficulties arise. The shower is produced farther away from the telescopes for larger zenith angles, which means the Cherenkov light has to travel a longer way through the atmosphere and experiences more absorption and scattering on the way[3]. Additionally the energy threshhold for a detection with MAGIC is higher because only the most energetic gamma rays will produce air showers with enough Cherenkov radiation to survive the long way through the atmosphere. There are only a few sources that emit these VHE gamma rays and therefore can be observed at VLZA. However, the area of the Cherenkov lightpool increases at large zenith angles. This is due to the cone traveling a longer way, having more time to expand before hitting the ground. Therefore the probability for the light to hit our detectors is increased and so is the probability to detect VHE gamma rays from some selected sources. With this technique the MAGIC collaboration wants to study the highest energy gamma rays emitted by so-called PeVatron candidate sources [31].

It is clear that transmission values for the correction of the gamma-ray energy are especially important for VLZA observations. The used laser has a power of $5\,\mu$J per shot, which limits the reach of LIDAR measurements to a range of 25km into the atmosphere. Measurements with LIDAR are the preferred approach for small zenith angles, in order to get a profile of the atmospheric transmission, not only the integral value. But at VLZA the development of the shower happens outside of the laser reach. Therefore the LIDAR cannot operate at zenith angles larger than $60\,^\circ$. The MAM telescope was installed on La Palma with the goal to compensate for this and measure the transmission during VLZA observations[4]. In the next chapter this subsystem is introduced.

[3]Absorption and scattering of light are described in more detail in section 3.2.

[4]At large zenith angles the integral transmission of the atmosphere is a good approximation for the part that has to be overcome by the Cherenkov light.

2 The MAM

The MAM telescope is located next to the first-built of the two MAGIC Telescopes (MAGIC 1) at the Roque de los Muchachos European Northern Observatory on La Palma, Canary Islands, Spain. It is situated inside of the fenced area of MAGIC 1 and was operated remotely for this Bachelor thesis. The following subsections introduce the task and the hardware and software components of the MAM subsystem, shown in Figure 3.

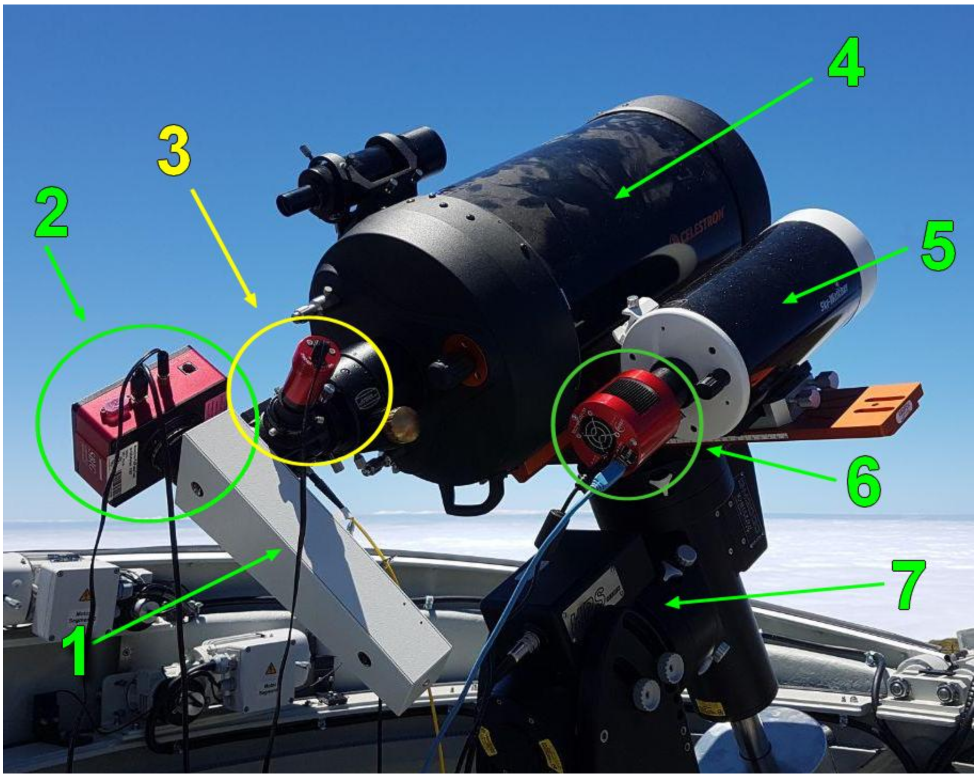

Figure 3: The MAM telescope on site in La Palma. 1: Spectrograph, 2: SBIG camera, 3: Slit camera from ZWO, 4: 11-inch telescope from Celestron, 5: 5-inch telescope from Skywatcher, 6: ASI1600mm camera for the photometry, 7: 10micron mount.

2.1 The task of MAM

The (long-term) plan for the MAM telescope is to measure the transmission of the atmosphere in real time in the pointing direction of MAGIC and especially during VLZA observations. This task can be accomplished with photometry or with spectroscopy by measuring the brightness or the spectrum of a star and comparing the results to reference magnitudes[5] or spectra. MAM is equipped for both possibilities, but it is photometry that was used in this Bachelor work. The special requirements for observations with MAM imply several aspects for the implementation:

1. For every MAGIC target (that is observed at VLZA) a close-by star, which can be used for photometric measurements, has to be selected. It should be bright enough and non-variable.
2. To calculate the transmission a reference magnitude of the observed star is needed, which can be used for comparison of the measured magnitude.
3. The measurement of transmission should happen in real time, in order to enable the operators of MAGIC to judge if an observation is worth to be continued.
4. The goal is to move towards a mostly automatic/robotic mode of operation with MAM.

Possible realizations of these requirements will be explained in section 3.7, and will be reviewed at the end of the thesis, taking into account the results.

2.2 Hardware

Hardware that was installed for the MAM includes a 10micron mount, two telescopes (11-inch Schmidt-Cassegrain telescope from Celestron and 5-inch Maksutov-Cassegrain telescope from Skywatcher), 3 cameras and a filter wheel, an Echelle spectrograph, and a Baader dome. For this Bachelor thesis only the small 5-inch telescope, filter wheel from Baader, and ASI1600mm cooled camera from ZWO were used and will be described. Details on the rest of the equipment can be found in the preceding Master's thesis [13].

The filter wheel from Baader contains four filters for the luminance (L), red (R), green (G), and blue (B) band of the spectrum. Figure 4 shows their transmission curves. Although they are called L-RGB in the image they will be denoted with l, r, g and b for the rest of this thesis to avoid confusion with the Landolt filters UBVRI. The l filter curve approximately covers the other three curves of the r, g, and b filters.

For this project an ASI1600mm cooled monochrome camera was used. Technical specifications can be found in appendix B. The typical detector for photometric measurements is a CCD (Charged Coupled Device) chip, but the ASI camera has a CMOS (Complementary Metal-Oxide Semiconductor) chip. CCD cameras read out the pixel charge line-wise by shifting the charge to one side successively, whereas CMOS pixels are read

[5]The actual steps for calculation of the transmission and the quantity magnitude are explained in section 3.3. For now and for all following use cases of the word magnitude that come before the definition, it is sufficient to know that a magnitude is a value describing the brightness of an object.

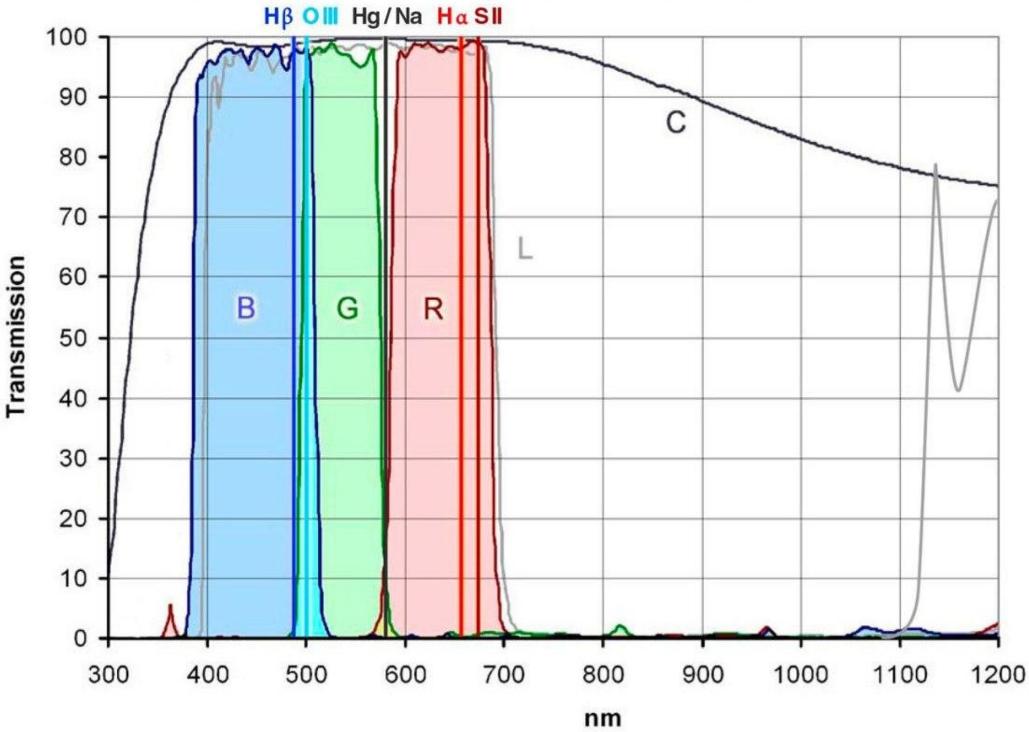

Figure 4: Transmission curves for the 4 Baader filters L-RGB, in the following denoted l, r, g and b to avoid confusion with the Landolt filters UBVRI. The x-axis displays the wavelength in nm. The curve for the l filter (in light gray) essentially covers the sum of the other three filter curves. Plot taken from [2].

out individually all at the same time. Although the readout process is different, the basic principle of both types of sensors is the same: Counting the photons that fall onto it. The crucial part about that counting process is that each pixel can only count a limited number of photons. The counts are called ADUs (Analog-to-Digital Units). At some point the accumulated charge in one pixel gets saturated. If this happens, newly arriving photons will not be counted any more, even if the exposure continues. It is important to stay in the linear region for photometry, otherwise no reliable statement can be made about the brightness of an object, because the relation between incoming photons and detected charge will be unknown. The camera has a 12 bit Analog-to-Digital Converter (ADC), which means that it saturates at a count of $2^{12}\,ADU = 4096\,ADU$. The maximum of ADUs which can be found in the images afterwards is actually much higher, because the 12 bit value is internally converted to 16 bit, meaning that every value is multiplied by $2^4 = 16$. That last part is an unusual feature, a peculiarity of the camera. For this 16 bit design the suitable region for photometry lies below 40,000 counts. The useful region for measurements is also limited by the Signal-to-noise Ratio (SNR), explained in section 3.4. To achieve a sufficiently strong signal of a source the maximum count should be above 20,000 ADUs. Observations were therefore carried out between 20,000 and 40,000 counts (see section 4.1).

2.3 Software

The software for the control of the telescope is described in [13], the source code can be found in a git repository [14]. It is written in python and makes use of standard modules like numpy and scipy, astronomy modules like astropy, astroquery, ccdproc and zwoasi. The last is a package used to control the ZWO camera. For the moment, no graphical user interface exists, instead the telescope is controlled using the console and several commands. During this Bachelor work I implemented several new modules and commands, which will be useful for a future automatic mode of operation. Details of the modules written and used for the analysis are given later on in section 4.1.

3 Theory of photometric measurements and a concept for MAM

Photometry describes the process of measuring the flux an object emits depending on the wavelength. Sometimes also the temporal nature of the flux can be of interest, e. g., when determining a flux curve from a variable star or - which is closer to the related topic - from a blazar (see section 1.1), since they are highly variable objects. Generally two kinds of photometric concepts can be distinguished, relative (or differential) and absolute photometry. The former approach does not look at absolute fluxes of stars but only at differences of fluxes. For instance, a target of observation and a close-by non-variable reference object are measured at the same time to determine the variability characteristics of the target object. This kind of photometry benefits from the fact that the observing conditions for the compared objects are very much the same because of the positional and temporal proximity of the measurement. This implies that many effects, otherwise considered fatal for the usefulness of the data, are not so much of a problem, for example thin cloud layers. They affect both target and reference object and will be cancelled out in the relative values. Absolute photometry on the other hand has the goal to determine the total flux of a star or other astronomical object. This requires to correct for certain effects like atmospheric extinction. Since absolute photometry is needed for measuring the transmission the next subsections will give an overview about photometric filter systems and atmospheric extinction.

3.1 Photometric systems and the Landolt catalog

Photometry is sometimes considered as low-resolution spectroscopy, because it makes use of narrow-, intermediate- and broad-band filters with spectral widths of less than 10 nm up to more than 100 nm to determine the brightness of a celestial object. There exist a big number of different (standard) photometric systems extensively described by Bessel [4]. The most widely utilized broad-band photometric system today is the $\mathrm{UBVR_cI_c}$[6] Johnson-Kron-Cousins system. Johnson and Morgan developed the original UBV filtersystem in 1953 [19], which is based on the star Vega of spectral type A0, and extended it to longer wavelengths in 1966, called UBVRI Johnson system [18]. With the development of new red-sensitive photomultiplier tubes (PMTs) and later of CCD cameras the original RI filters used by Johnson became inappropriate. The more precisely standardized $\mathrm{R_cI_c}$ Kron-Cousins system is used more frequently nowadays [4].

The catalog that is used in this Bachelor work is the Landolt catalog of standard stars from 1992 [25]. Landolt's work was based on the $\mathrm{UBVR_cI_c}$ system. For the rest of this Bachelor thesis I will denote the Landolt filters with UBVRI for convenience. His goal

[6] U for ultraviolet band, B for blue band, V for visual band, $\mathrm{R_c}$ for red band, $\mathrm{I_c}$ for infrared band. The subscript *c* indicates the Cousins system.

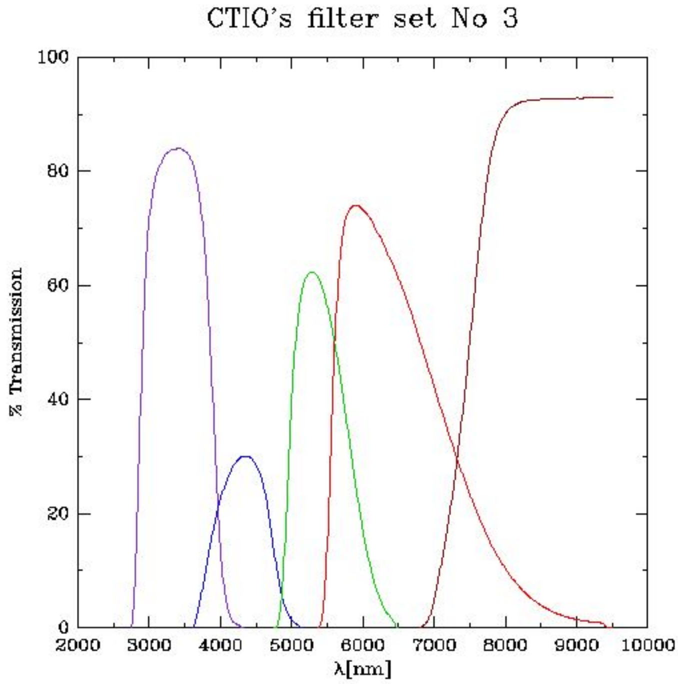

Figure 5: Transmission properties of the UBVRI filters used by Landolt. Plot of transmission in % against wavelength λ in nm. The violet, blue, green, red and brown curve are the transmission curves of filters U, B, V, R and I, respectively. The graph was produced using the services of the Strasbourg astronomical Data Center [42].

was to provide a large and internally consistent set of faint standard stars across the sky. From the Kitt Peak National Observatory he repeatedly observed different selected areas around the celestial equator in the UBV bands. The fields contained a total of 642 standard stars of all colors. For details on the program see [23]. In following years he extended his photometry to UBVRI photometric observation and refined and updated the catalog several times [24, 25, 26, 27]. Figure 5 shows the transmission curves of the UBVRI filter set that was used for the Landolt catalog.

There are several important facts to know about photometric filter systems:

1. No photometric system is the exact copy of another, even if the filters are of the same type there can be slight differences in the transmission properties. This is the reason for the need of transformation relations between photometric systems, otherwise measurements with different equipement and photometric filters cannot be compared and evaluated together. An example is that Landolts U and B filter were not as good a match to the Johnson system as Cousins filters were. This lead

to inconsistencies between the Landolt and Cousins UBVRI system [4].

2. Not only the transmission of filters is relevant to be able to profit from the high precision of standard systems. The response function of the detector is equally important, because it defines which wavelengths of light are detected. The observable band resulting from the combination of both filter transmission properties and the wavelength dependent sensitivity of the detector is called a passband. The problem is the following: Even if the transformation to a standard system is precisely determined using a set of standard stars, the transformation might not be applicable to other stars (of different color). Bessel accurately describes it as follows:

   "...[T]wo observers using different passbands may achieve well-defined and precise transformations for the standard stars but will find large differences for their program objects which have spectra dissimilar to the standards." (p. 1181, [3])

   The conclusion I make for my work is that stars with a wide range of color indices (color indices will be explained in section 3.2.2) should be used for the photometric calibration to ensure applicability of the transformation to other stars of the catalog.

3. The central wavelength of a filter is not necessarily the same as the effective wavelength. As shown in Figure 6, the effective wavelength of a filter depends on the spectral properties of a star. With reference to the next subsection this is the reason for a color dependent term of the extinction coefficient and will be explained there.

To be able to compare MAM measurements of standard stars in different filters with the results from Landolt or other photometric systems, a transformation relation between similar filters has to be determined. In this case the r filter magnitude of a star in the MAM photometric system (Baader system) will be a function of the R filter magnitude in the Landolt system, and analogous for filter pairs g/V and b/B in the Baader/Landolt system. It will enable the calculation of the transmission in different wavelength bands corresponding to the three Baader filters.

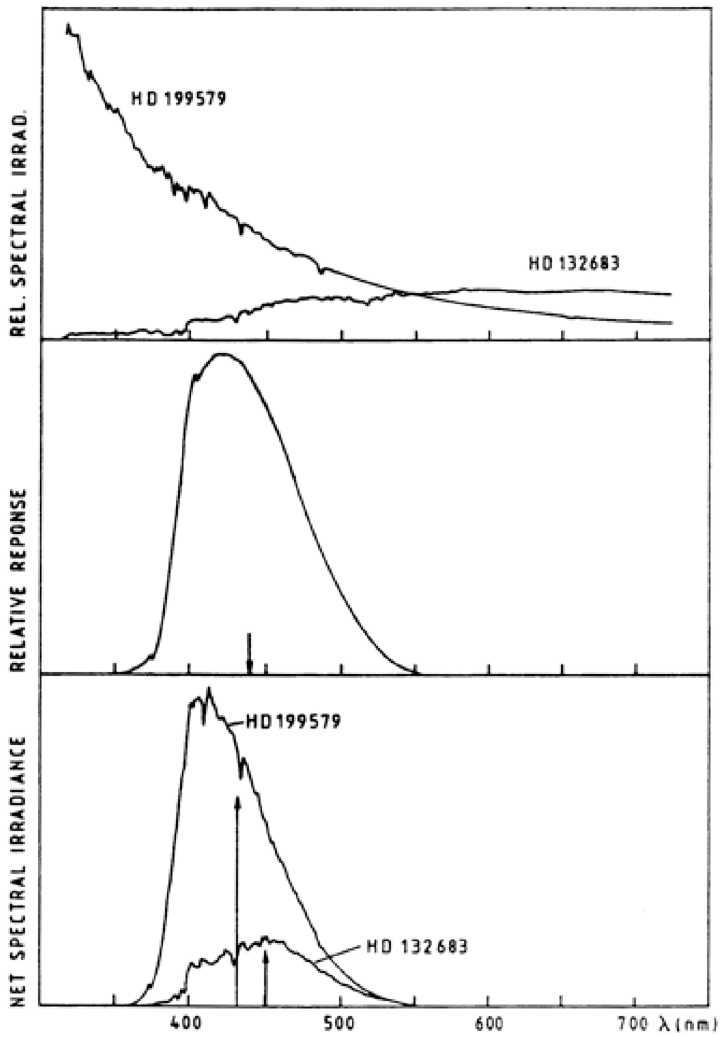

Figure 6: The plots show the spectral emission of two different stars (top), the transmission (or response) curve of a broad-band filter (middle) and the spectral emission an observer will measure for the two stars, by applying the filter (bottom). On the x-axis is the wavelength λ in nm. The central wavelength of the filter and the effective wavelength of the filter for different target objects are marked with arrows in the middle and bottom panel, respectively. It is clear that they are not the same for stars of different color. This is the reason for the color dependent term of extinction (see section 3.2.2). Graph taken from [17].

3.2 Atmospheric extinction

When doing earth-bound photometric measurements, the most unavoidable topic to study is atmospheric extinction. The term denotes the dimming of light, which passes through the atmosphere, and has many closely related or synonymous terms, including airmass, optical thickness and absorption. It is wavelength dependent and caused mainly by two effects, which are the scattering and the absorption of light.

3.2.1 Zenith angle and airmass

A short explanation of the zenith angle (or zenith distance) is given here, because it will be used frequently throughout the thesis. In astronomy, one of the most important coordinate systems is the horizontal coordinate system. In this system, a star's position is described by two angles, the altitude angle (Alt) and the azimuth angle (Az). Alt simply contains the altitude of a star above the horizon. The zenith angle is:

$$Z = 90\,^{\circ} - Alt. \tag{1}$$

For different zenith angles, the observing conditions change because of the Earth's atmosphere. More layers of atmosphere between the star and the observer will result in more dimming of light. Therefore we need a quantity to describe through how much air the light has travelled when arriving at the detector, independent of the weather conditions. This quantity is called airmass (AM), its mathematical name typically is X. By definition, an observer looking straight up at the zenith (zenith angle $Z = 0\,^{\circ}$) encounters an airmass of 1 in his line of sight. Moving to higher zenith angles, the airmass first increases slowly, then quickly as it approaches the horizon. For the approximation of a flat Earth and atmosphere, shown in Figure 7a, the airmass X can be written as a function of the zenith angle Z [40]:

$$X \approx \sec(Z). \tag{2}$$

This approximation is very close to the correct values for up to $60\,^{\circ}$ zenith angle and is used in this Bachelor thesis. Below that the curved form of the atmospheric layer cannot be neglected any more, see Figure 7b. Several approximation formulas are known to give reasonable results in this case. For my observations above $60\,^{\circ}$ zenith distance I use the formula derived by Kasten and Young [21]:

$$X = [\cos(Z) + \frac{0.50572}{(6.07995 + 90 - Z)^{1.6364}}]^{-1}. \tag{3}$$

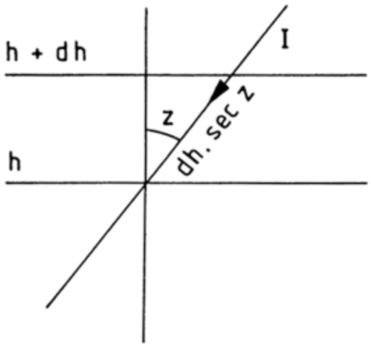

(a) Geometrical construction of airmass for the approximation of a flat Earth and atmosphere. z is the zenith angle, h is the height above the ground and dh is an infinitesimal change in height. The arrow shows the direction of the incoming light.

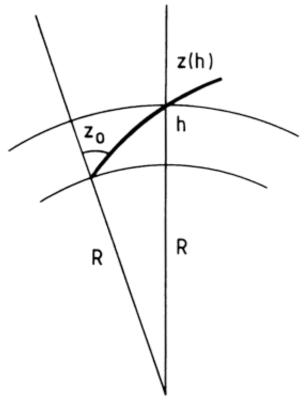

(b) Geometrical construction of airmass for the real, curved atmosphere of the Earth. z stands for the zenith angle, h for the height above the ground and R for the Earth's radius. Two effects can be seen: At high zenith angles the light has to overcome more layers of atmosphere and it travels on a curved path because of the atmospheric refraction effect.

Figure 7: Geometrical construction of the quantity airmass. Images taken from [17].

In the following, the expression 'magnitude at airmass zero' will denote the magnitude of a star that would be measured if there was no atmosphere (which corresponds to airmass zero).

3.2.2 Transmission and extinction coefficient

The longer starlight has to travel through the Earth's atmosphere before falling onto a detector the fainter the star image will be. This can be described with the following equation:

$$F = F_0 e^{-\tau X}. \tag{4}$$

The total flux F_0 of a star in units of s^{-1} is the number of detected photons per second. The use of intensities instead of fluxes or any other flux unit gives a formula equivalent to this one. F_0 is dimmed exponentially, depending on the optical depth τ of the atmosphere and the airmass X, resulting in an observed flux F. The fraction of the starlight reaching the observer is known as the transmission T,

$$T = \frac{F}{F_0} = e^{-\tau X}. \tag{5}$$

This is the quantity we are interested in with the measurements of MAM, once a reliable photometric transformation relation between the Landolt and the Baader system is known. The concrete calculation of the transmission with MAM in the future will be explained in section 3.3.

During the photometric calibration, the extinction at the Roque de los Muchachos on La Palma will be determined. Mathematically it is characterized with the extinction coefficient κ_λ. The coefficient is wavelength dependent, but the mathematical relation for this dependency will be introduced in the next subsection. As explained in section 3.1 and shown in Figure 6, the effective wavelength and the central wavelength of a filter are not necessarily the same for stars of different color. The color index of a star is the magnitude difference between two bands computed by subtracting the magnitude at longer wavelengths from the magnitude at shorter wavelengths (for example $(B-V)$ or $(V-R)$). A smaller or more negative value therefore indicates a bluer star. The extinction coefficient measured in a certain broad-band filter also depends on the color index C of the observed star. The color dependency can be written as:

$$\kappa_\lambda = \kappa_{\lambda,1} + \kappa_{\lambda,2} C. \tag{6}$$

$\kappa_{\lambda,1}$ and $\kappa_{\lambda,2}$ are the primary and secondary extinction coefficient, respectively [28, 17]. The second term represents the color dependent term of extinction. The primary extinction coefficient is known to show seasonal variation, whereas the secondary extinction coefficient is a relatively stable quantity [28, 6]. In this work I will only determine a mean overall extinction value for every passband. The sample of stars that was observed is not enough to determine the primary and secondary extinction coefficients with a linear fit.

3.2.3 Causes of extinction

Having defined the extinction coefficient mathematically, this section will give the wavelength dependency and physical explanations of extinction. As shown in Figure 8, there are three main components: Scattering of light on air molecules or other particles, including Rayleigh scattering and aerosol (Mie) scattering, and absorption of light by molecular bands. In most cases the Rayleigh scattering makes up the biggest part of extinction for blue light, then comes the aerosol scattering and then the absorption which is essentially due to ozone. For the red part of the spectrum the contribution of aerosol scattering becomes more influential. However, the last two statements depend on the aerosol concentration in the air and cannot be claimed for the general case. Like

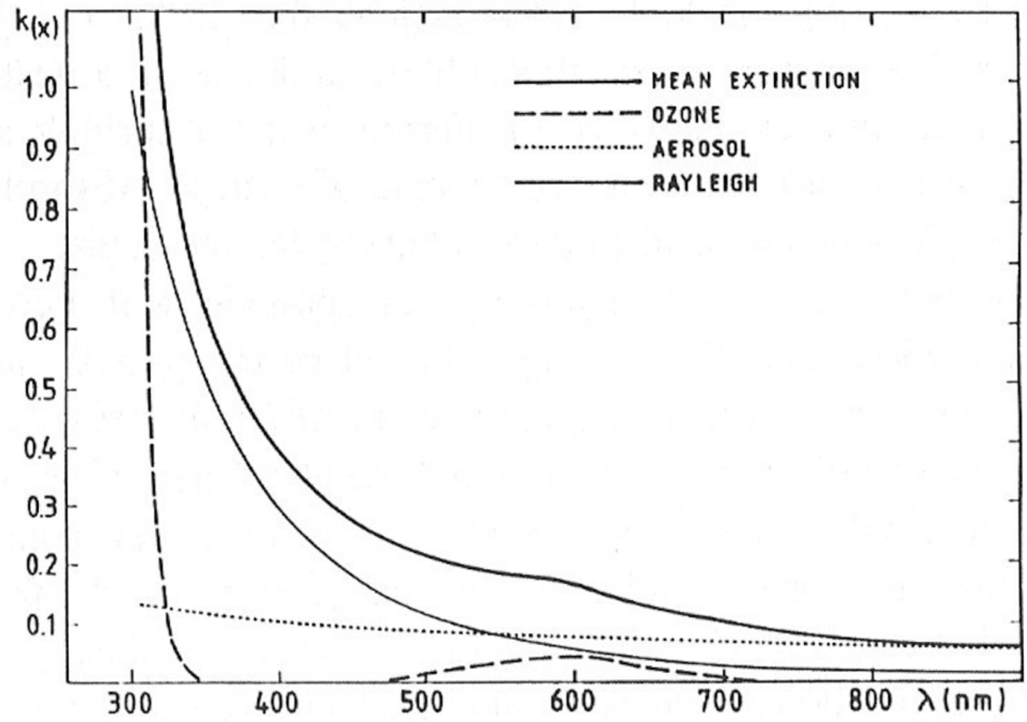

Figure 8: The plot shows the contributions of the three main components of extinction in the Earth's atmosphere to the integral extinction. On the x-axis is the wavelength in nm, on the y-axis the extinction coefficient κ_λ. The three components of extinction are Rayleigh and aerosol scattering and absorption of light in the atmosphere (mainly by ozone). The dominating effect will depend on the aerosol concentration, but blue light generally is more affected by Rayleigh scattering. Rayleigh scattering is nearly constant over time and only shows a slight seasonal variation, whereas aerosol scattering is influenced by many processes in the environment. The strong wavelength dependency of Rayleigh scattering is transferred to the overall extinction. Therefore blue light is dimmed a lot more than red light. Graph taken from [17].

the extinction itself, the scattering efficiency is a function of wavelength, therefore the wavelength dependency of the extinction coefficient $\kappa(\lambda)$ can be expressed as [28]:

$$\kappa(\lambda) = \frac{\beta}{\lambda^{\mathrm{n}}}. \tag{7}$$

β and λ represent a constant and the mean wavelength of a filter, respectively. The law describes different kinds of scattering depending on the exponent n. According to Burki [6] and Lim [28], the aerosol scattering has an exponent n between 1 and 2, and for the Rayleigh scattering n becomes 4. This relation is depicted in Figure 9. Aerosols contribute less to the extinction in the blue part of the spectrum than Rayleigh scattering but their contribution, unlike the one by Rayleigh scattering, cannot be easily calculated or modeled. Some telescopes, like the F/(Ph)otometric Robotic Atmospheric Monitor (FRAM) and the Atmospheric Research for Climate and Astroparticle DEtection Raman LIDAR (ARCADE RL), both located on La Palma as well, are designed to measure the Vertical Aerosol Optical Depth (VAOD) [8]. In the last section the optical depth τ was introduced. FRAM measures the integral optical depth of the atmosphere and then removes the contribution of the Rayleigh scattering and absorption, leaving only the aerosol optical depth. The contribution of Rayleigh scattering and absorption are derived from meteorological data [8, 35]. During the measurement for this Bachelor thesis, both ARCADE and FRAM took data. I used this data (which was communicated personally) to crosscheck the weather conditions reported by the LIDAR (see section 4.1).

In Figure 9 the open squares, filled circles, open circles, and filled squares represent the mean extinction coefficients in spring, summer, fall, and winter, respectively. The relation clearly shows another influence on extinction, which is the season of the year. At the site of the Maidanak Astronomical Observatory (Uzbekistan) extinction was found to be highest in spring and summer, lowest in winter. Observatorys at other sites have found similar results on the seasonal variations. Long term studies of extinction at the La Silla Observatory (Chile) of the European Southern Observatory (ESO) have found the highest extinction values in austral summer. This is explained by a high atmospheric reversing layer during the season [6]. For Figure 10, the long-term variation of the extinction coefficient was monitored in the UBV bands. The two unusual bumps in the curves were caused by volcanic eruptions that took place in 1982 in Mexico (El Chichon) and 1991 on the Phillipines (Pinatubo). In both cases, an obvious increase in extinction, that lasted up to 3 years or more, can be observed [6]. Because the site of La Palma is especially interesting for this Bachelor thesis, I also included another long term measurement campaign by the Carlsberg Meridian Telescope (CMT), located in La Palma since 1984. This is shown in Figure 11. Similar to extinction at La Silla the measurements at the CMT show a higher extinction in summer. Helmer attributes this to the frequent high dust concentrations in the air, caused by Calima (sand-laden wind from the Sahara desert) [12]. The extended period of high extinction after the eruption of Pinatubo in 1991 was clearly detected in La Palma (see Figure 11).

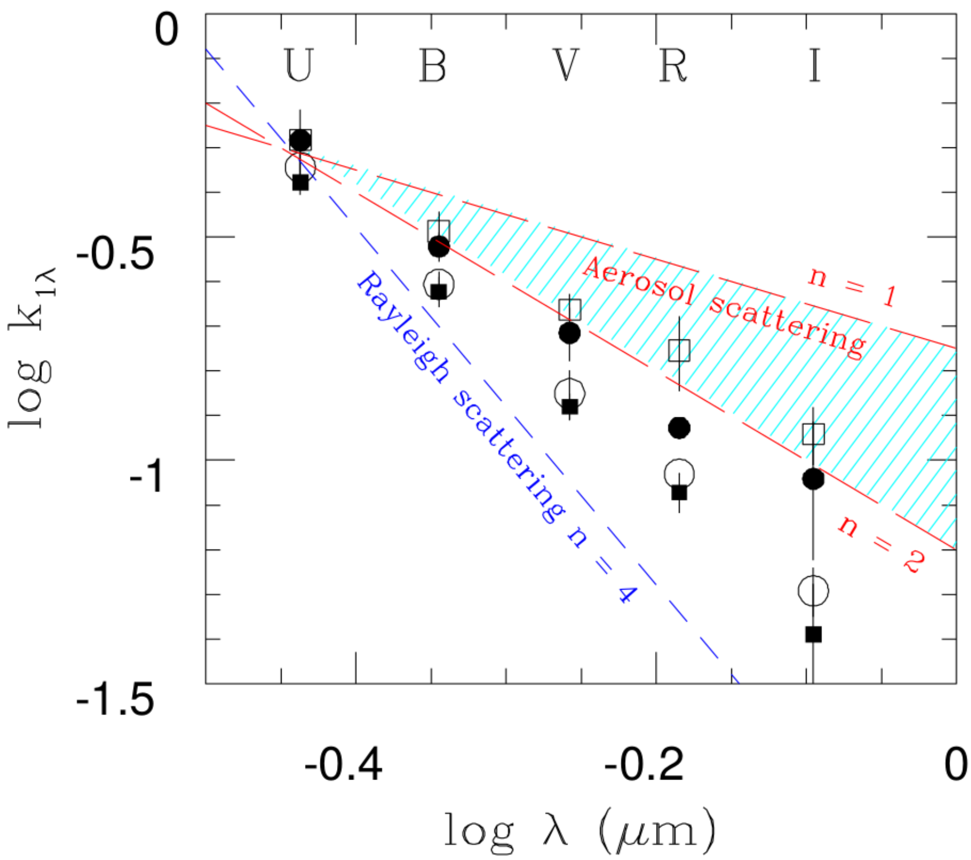

Figure 9: Relation between mean extinction coefficient for a given season and the wavelength of the light, measured at the Maidanak Astronomical Observatory (MAO) in Uzbekistan. The two long-dashed lines mark the limits of the area, that is affected by aerosol scattering and the blue line represents the Rayleigh component. The open squares, filled circles, open circles, and filled squares represent the mean extinction coefficients in spring, summer, fall, and winter, respectively. A clear seasonal effect can be seen, with more impact on the red part of the spectrum. In spring the extinction is high and has a strong aerosol scattering component (expected to be the influence of dust), in winter the air is very clear and the extinction dominated by pure Rayleigh scattering. Plot taken from [28].

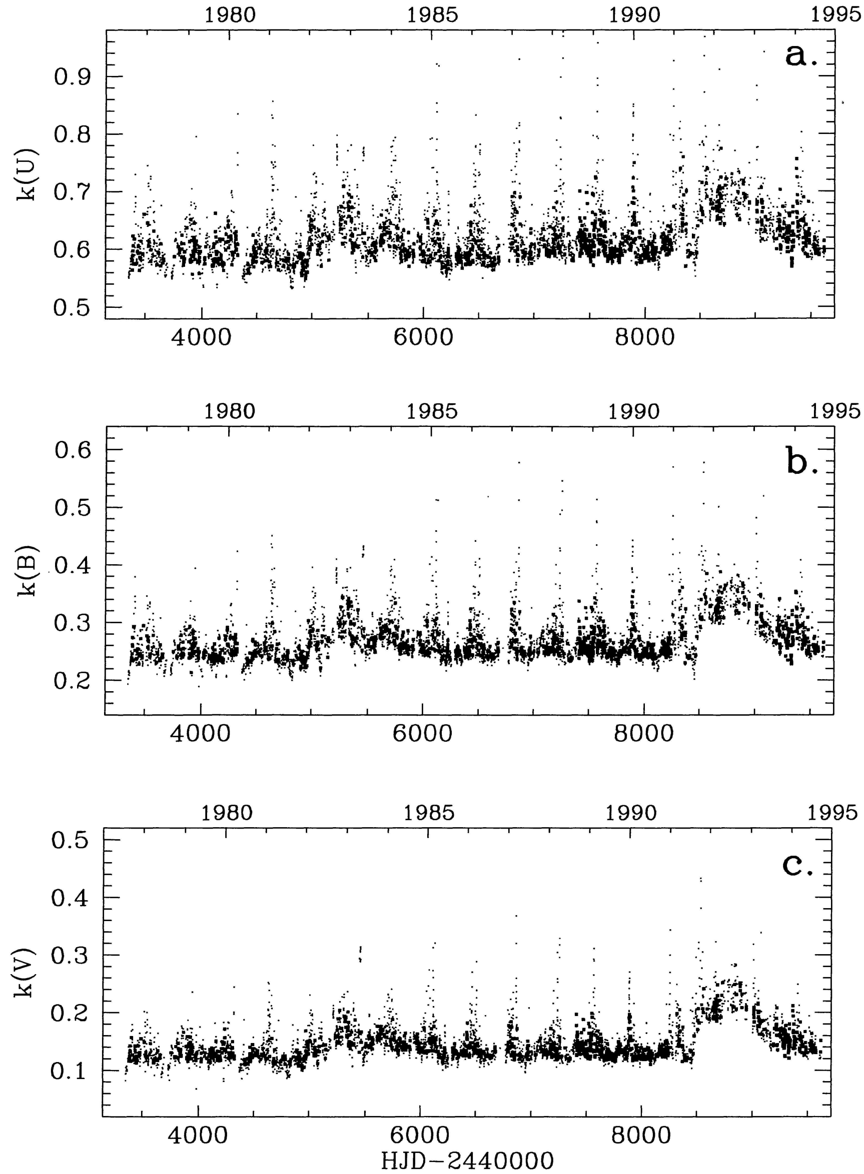

Figure 10: Variations of the extinction coefficients in the U, B and V bands from 1978 to 1995 at the ESO La Silla Observatory. An obvious seasonal variation is shown. The two striking bumps were caused by two volcanic eruptions, El Chichon in Mexico in 1982 and the Pinatubo on the Phillipines in 1991. They filled the atmosphere with volcanic aerosols and ash particles, which reached La Silla roughly 150 days and 100 days after the eruption in the case of El Chichon and Pinatubo, respectively. Plot taken from [6].

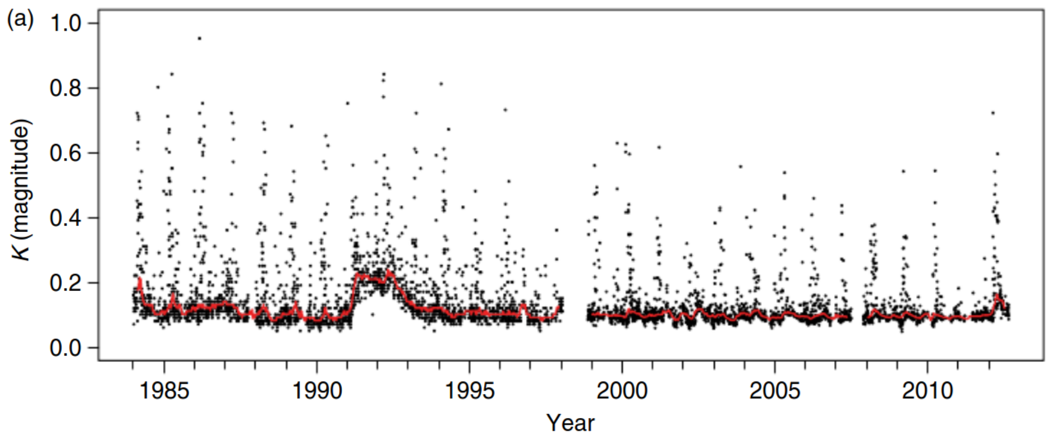

Figure 11: Atmospheric extinction values in red band (central wavelength 625 nm) in units of magnitude for La Palma between 1984 and 2012. The red line is computed from 100-day median values. The measurements were taken with the Carlsberg Meridian Telescope (CMT). Like in Figure 10, a seasonal variation of the (mean) extinction coefficient can be seen, being higher in summer than in winter. The period of high extinction after the eruption of Pinatubo was also registered on La Palma and corresponds to the bump between 1990 and 1995. The minimal mean extinction value can be estimated to lie at 0.1 magnitudes. Plot taken from [22].

Apart from the mentioned, there are other processes and factors influencing extinction, for example the aerosols and ashes from wildfires, absorption by oxygen and water, and quite importantly the height of the observing site (more on that can be found in section 4.2.4). The main goal of this section was to point out the variation of the extinction coefficient, with time, with location, with wavelength and with the color of an observed star. It is crucial to be aware of these effects in order to give a correct interpretation of photometric measurements. Some important concepts for a photometric calibration will be explained in the next section.

3.3 Instrumental magnitude, zero point and color term

The magnitude of a star or other object is a quantity for its brightness. Astronomy knows two kinds of magnitudes, the absolute magnitude and the apparent magnitude. The first contains the brightness of an object, normalized to a certain distance between the observer and the object. In order to compare the brightness of different objects this normalization is needed, because a star beeing farther away from the observer will appear fainter. The second is the magnitude an observer measures from the Earth. In the following the use of the word magnitude will always mean the apparent magnitude. The magnitude difference Δm of two objects is proportional to the logarithm of the ratio of their fluxes F_1 and F_2[7]:

$$\Delta m = m_1 - m_2 = -2.5\log(\frac{F_1}{F_2}). \tag{8}$$

In accordance with the ancient magnitude system, the physical definition of magnitudes was adapted to be representative for the visual response of the human eye, which is roughly logarithmic [30]. This lead to the factor of 2.5 in Equation 8 and means that five magnitude steps correspond to a factor of a hundred in brightness. It also implies that smaller or more negative magnitude values indicate brighter objects: Our Sun has a magnitude of $m_{\text{sun}} \approx -26$, our Moon has a magnitude of $m_{\text{moon}} \approx -12$, and the brightest stars in the sky have magnitudes starting from $m_{\text{star}} \approx -1$. Reversing the above equation and replacing the fluxes F_1 and F_2 of different stars by two different fluxes F (measured) and F_0 (total flux outside the atmosphere) of the same star gives:

$$T = \frac{F}{F_0} = 10^{-0.4\Delta m}. \tag{9}$$

This is the same definition for the transmission T as in Equation 5, but rewritten in terms of the magnitude difference Δm between the measured magnitude of a star and the reference magnitude of a star at AM zero. It will be used for measurements with MAM in the future.

The definition for a single magnitude is called the instrumental magnitude because it depends on the observing system. The outcome of the data reduction and analysis of one image will be the total number of ADUs N_{ADU} generated by photons from the target star. This value is converted to the instrumental magnitude m_{instr} of the observing system:

$$m_{\text{instr}} = -2.5\log(\frac{F}{g}) = -2.5\log(\frac{N_{\text{ADU}}}{tg}). \tag{10}$$

Before taking the logarithm we need to convert the number of counts (ADUs) into a flux value by dividing with the exposure time t of the measurement in seconds. Longer exposures make the star appear brigther than short ones. The magnitude however is independent of this duration and therefore we have to normalize with the exposure time. Now we have a flux of counts (ADUs) per second and need to divide by the gain g in units of e^-/ADU, because it describes how many electrons are needed to produce one ADU. For the measurements with MAM, a gain setting of $1\,e^-$/ADU was used. To find a relation between the instrumental magnitude and the actual catalog magnitude of a

[7]Formulas in this section are from [17], [5] and [33].

star (both at AM zero) several corrective terms and factors have to be applied, involving the correction for the atmospheric extinction. The corrected relation can be obtained by taking the logarithm of Equation 4 [17]:

$$m_{\mathrm{instr,0}} = m_{\mathrm{instr}} - \kappa X. \tag{11}$$

$m_{\mathrm{instr,0}}$ denotes the instrumental magnitude at AM zero. With a number of observations of the same star at different airmasses the extinction coefficient κ and $m_{\mathrm{instr,0}}$ can be obtained in a simple way:

$$m_{\mathrm{instr,i}} = m_{\mathrm{instr,0}} + \kappa X_i. \tag{12}$$

Plotting a set of instrumental magnitudes $m_{\mathrm{instr,i}}$ against a set of airmasses X_i and fitting a linear curve to them yields the slope and the y-axis intercept, which correspond to κ and $m_{\mathrm{instr,0}}$, respectively. In this way the measured intrumental magnitudes were extrapolated to AM zero in the analysis (section 4.2.4).

The amount of light reaching the sensor is also influenced by the transmission and reflectivity properties of filters, mirrors and lenses. This means that every photometric system will have an individual instrumental zeropoint *ZP*, which needs to be determined in order to compare a measured instrumental magnitude m_{instr} at AM zero to a reference magnitude m_{lit} at AM zero. The subscript 0 for AM zero will be omitted for the rest of this section. The use of the word magnitude will always mean the magnitude at AM zero. Also note that the zeropoint of a system is not constant over time but changes gradually, mostly due to accumulating dust on the surface of mirrors and lenses [28]. For repeated photometric measurements a new zero point has to be determined regularly.

The relation for a certain filter f between literature magnitude m_{lit} and instrumental magnitude m_{instr} depends on the following quantities: The color transformation coefficient a, a related color index C and the zero point *ZP*. The related color index means a color index containing the magnitude in filter f. The magnitude transformation [28, 5, 41] can be rewritten as a set of equations, with the index i denoting different stars,

$$m_{\mathrm{lit}} = m_{\mathrm{instr}} + ZP + aC, \tag{13}$$

$$m_{\mathrm{lit,i}} = m_{\mathrm{instr,i}} + ZP + aC_{\mathrm{i}}. \tag{14}$$

To find the unknown parameters *ZP* and a, a least squares solution was determined with the χ^2-fitting method (see next paragraph). Correctly speaking Equations 13 and 14 are only approximations. There are other terms of higher order, which are often neglected because they are expected to be quite small [20, 37]. The cases for an additional second order term are

$$m_{\text{lit}} = m_{\text{instr}} + ZP + a_1 C + a_2 C^2, \tag{15}$$

and

$$m_{\text{lit,i}} = m_{\text{instr,i}} + ZP + a_1 C_{\text{i}} + a_2 C_{\text{i}}^2. \tag{16}$$

a_1 denotes the transformation coefficient related to the linear term of the color index C_{i} of a star and a_2 denotes the transformation coefficient related to the quadratic term of the color index C_{i}^2 of a star. As in Equation 14, a least squares fit can be found for the three parameters *ZP*, a_1 and a_2 taking into account the uncertainty of the measured quantities $m_{\text{instr,i}}$. In both the linear and the quadratic case the χ^2-minimization was applied. The method defines a quantity

$$\chi^2 = \sum_{i=1}^{N} \frac{(x_{\text{i}} - y_{\text{i}})^2}{\sigma_{\text{i}}^2}, \tag{17}$$

and then minimizes it by taking the derivative and setting it equal to zero. It is a sum over the squared differences between a measurement x_{i} and an expected value y_{i}, weighted with the uncertainty of the measured quantity σ_{i} squared. N is the total number of datapoints. Substituting the general expressions in Equation 17 with the terms in Equation 14 or 16 yields the concrete χ^2-function for the case of the linear or quadratic transformation relation:

$$\chi^2 = \sum_{i=1}^{N} \frac{(y_{\text{i}} - (ZP + x_{\text{i}} + a_1 C_{\text{i}}))^2}{\sigma_{\text{i}}^2}, \tag{18}$$

$$\chi^2 = \sum_{i=1}^{N} \frac{(y_{\text{i}} - (ZP + x_{\text{i}} + a_1 C_{\text{i}} + a_2 C_{\text{i}}^2))^2}{\sigma_{\text{i}}^2}. \tag{19}$$

The derivation of the minimization for the quadratic case can be found in appendix A.2. The linear case is analogous, but quicker to solve. The results of the application of the χ^2-method to the linear and quadratic case will be discussed in section 4.2.5. Information on the χ^2-minimization can be found in [36].

A photometric transformation can also be written in terms of colors [27, 28]:

$$C = aC' + b. \tag{20}$$

$$C_{\mathrm{i}} = aC_{\mathrm{i}}^{'} + b. \tag{21}$$

$C^{'}$ is the color index from two measured instrumental magnitudes, C is the reference color index from a catalog, and a and b are the transformation parameters. Typically, transformation relations are given as a set of color transformations [25], with only one magnitude transformation as in Equation 13. For this Bachelor work I will determine the magnitude transformations for magnitudes in the r, g and b band and no color transformations. The reason is that we aim for calculation of the transmission, and the magnitude transformation between the two systems is exactly the information needed for this.

3.4 Data reduction theory

At this point some concepts of digital imaging with an electronic sensor have to be introduced that will be needed later. A CCD or CMOS image is influenced and disturbed by many effects. Caution during the capturing of images and proper data reduction can remove most of these with the help of calibration frames, like dark and flat frames. They will be explained in the following paragraphs.

Reliable measurements can only be done on an image, if the star of interest is set apart from the background by a certain amount of counts (ADUs). Otherwise it will drown in the background brightness fluctuations. To describe the strength of the source signal that is measured with respect to the combined noise (undesirable signal components produced by the device or the natural variation of the photon flux) a Signal-to-Noise Ratio (SNR) is defined:

$$SNR = \frac{S}{\sqrt{S + n_{\mathrm{pix}}(N_{\mathrm{s}} + I_{\mathrm{D}}t + N_{\mathrm{R}}^2)}}. \tag{22}$$

S is the total electron count[8] from the source (the signal), n_{pix} is the number of pixels for which the SNR is calculated, N_{s} is the total number of background sky electrons

[8] S can be written as $S = PQ_{\mathrm{e}}t$, where P is the photon flux in photons per second, Q_{e} is the quantum efficiency and t is the integration time in seconds [9]. It is important to understand that the measured quantities in a CCD or CMOS detector are always the electrons, no matter how many photons are statistically needed to excite one electron. In different definitions of the SNR the signal and other quantities are often expressed in terms of photons. This can be confusing, because what is actually meant is the number of electrons generated by the incoming photons. The relation between the number of photons statistically required to excite an electron (the quantum efficiency Q_{e}) is irrelevant. Consider having a mirror of double size but a quantum efficiency of only 1/4. The effective electron count would be the same. An absolute calibration of the energy is not needed because photometric measurements always refer either to a catalog or to measurements with the custom system (Q_{e} will be contained in the zero point of the transformation relation).

per pixel, I_D is the dark current in e^- per pixel per second, t is the exposure time in seconds and N_R is the read noise in e^- per pixel [15]. The denominator is the combined noise for all included pixels and can be considered as the uncertainty of the signal. There are three kind of noises, the photon (electron) noise $\sqrt{S}$ or $\sqrt{S + N_s}$ including the photons from the sky background, the dark noise (per pixel) $\sqrt{I_D t}$ and the read noise (per pixel) N_R. The photon noise results from the statistical variation of the arrival time of photons on a pixel. This noise follows the Poisson statistics [15]. The dark noise is produced by spontaneously generated electrons in the chip and is temperature dependent but independent of the photon-induced signal. The read noise is a result of the readout process, converting electron charge to a voltage signal. I will come back to the last formula later in section 4.2.3, to justify the error calculation for the calibration measurement.

The raw image data of a target object is called a light frame. The pixel count in such an image will not only contain the desired signal from the observed field, but also defects which can be isolated and removed afterwards. Most important effects include the dark current, the pixel-to-pixel variations in the CMOS response, a non-uniform illumination of the sensor, dust in the optical path and an underlying base level of counts, which is independent of the exposure time and results from the readout process[9]. The last is called the bias offset. An image with exposure time close to zero seconds and taken in total darkness will only contain this bias level and can be used to remove the constant offset in the light frames, by subtracting it. For the calibration measurement, I did not take bias frames but subtracted the bias level and dark current together, since the bias is also contained in the dark frame.

Another additive term in a light frame is the dark current in the sensor. It is produced by thermal excitation of electrons athough no light is falling on the sensor. Dark frames have to be taken in total darkness and with the exposure time of the light frame, because the dark current and number of hot pixels increase for longer integration times. Hot pixels are individual pixels which look much brighter than they should because of the incoming photons. They are a result of the dark current. It is important that the dark frames are taken for the same chip temperature as the light frames. The camera of the MAM can be cooled down to $-25\,°C$. Since there were problems with ice building up on the sensor plate, the camera was only operated at $-15\,°C$. This worked more or less fine for the dark frames. Typically 10 or more dark frames are captured instead of a single one. They are averaged before application to the light frame, in order to remove noise. Such an averaged dark frame is called a master dark frame.

Furthermore a calibration frame is needed, which will correct for the pixel-to-pixel variations, a non-uniform illumination of the sensor and dust in the optical path. This is the flat frame. The averaged version is the master flat frame. The light frame has to be divided by the averaged flat frame, because dividing by small pixel values (resulting from

[9]The readout requires the application of a small voltage to the pixels. Some electrons are excited by this readout voltage.

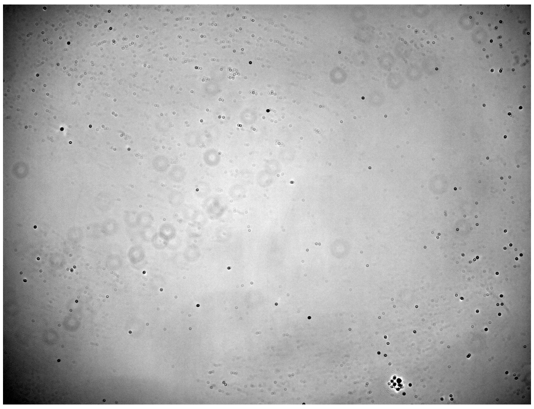

(a) Master flat frame in filter l

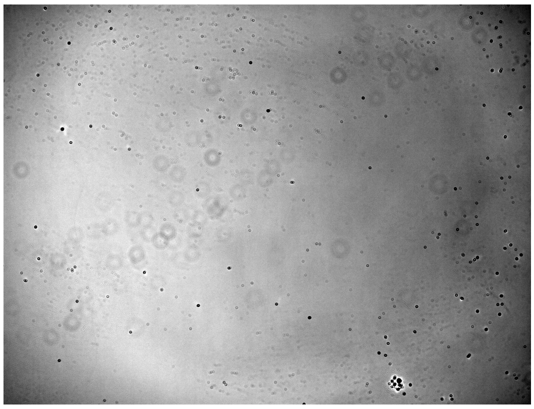

(b) Master flat frame in filter r

Figure 12: Two example master flat frames, each is the average of 20 flat frames taken with the MAM. It is clear that there is a difference between the transmission of filters l and r. Due to this variation every light frame has to be treated with a master flat frame of the corresponding filter.

vignetting or dust) will correct the brightness of the light frame upwards in the affected regions. For proper flat frames a uniformly illuminated background is needed. Good flat-fielding is the most difficult part of the corrections. There are several possibilities to do this: Sky flat frames are the most frequent among professional observers and are captured during dusk or dawn. An advantage is that the sky provides a very uniform illumination. For the special uses of the MAM, they are not well suited because they can only be taken in good weather conditions without clouds. MAM should also be able to operate and prepare an operation in imperfect weather conditions, therefore the flat frames taken during the Bachelor work were dome flats. Figure 12 shows two flat images from the measurement in different filters. They were taken by pointing the telescope to the inside of the dome. Two flat field lamps were installed in the dome in August 2020 and connected to a power switch in order to switch them on and off from remote. Since the dome wall is not perfectly uniform, a thin layer of white foam material was attached to one side of the dome shutter as a background for the flat-fielding. This worked well enough for the photometric calibration. References for all explanations about dark, flat and bias frames are [16, 5].

3.5 PSF photometry

PSF photometry is one possible approach to measure the brightness of a star. Except for a few very nearby stars, all stars are point sources. The point spread function (PSF) is the response of a focused 2D optical system to light coming from a point source. Mathematically, the convolution of the real light source with the PSF gives the image of the source. The PSF is dependent on optics, focus and tracking of a telescope. Assuming these factors to be of good quality, the major part of the point-spreading will be due to atmospheric seeing[10]. If the PSF (or a part of it) can be determined with a certain precision it can be used to measure the brightness of a star by integrating over the curve (or well chosen parts of it).

The PSF of an imaging system is in general unknown and can only be approximated. In theory, it has a symmetrical form and is perfectly circular, but this is not the case in reality. The PSF can take several other forms, e. g., elliptical form, depending on the quality of the optics and the seeing conditions. In an image, the PSF of different stars is the same apart from the amplitude scaling. A Gaussian function is a good description of the central part of the PSF[11] [7]:

$$I(r) = I_0 exp(-\frac{r^2}{2\sigma^2}). \tag{23}$$

I_0 is the intensity at maximum, r the distance from the star center, σ the width of the Gaussian. The flanks can better be approximated by a power law. Other functions exist that are also good models, e. g., a Moffat curve:

$$M(r) \propto \frac{1}{(1+\frac{r^2}{\alpha^2})^{\beta}}. \tag{24}$$

α and β are constants. The moffat curve is better than the Gaussian for approximation of the outer parts [33].

Relative photometry profits from positional and temporal proximity of target and reference measurement (as pointed out in section 3). In this case, a Gaussian can be used to fit the central part of both objects, then integrate the flux inside a certain aperture (the same aperture for both stars) and subtract both values. Since the PSF of both stars will only differ by a scaling factor and not by shape, the percentage of the total light enclosed in the aperture will be the same for both stars. This is the convenient way to avoid the problem of unknown flanks. It must be ensured however that the PSF shape does not change dramatically over the FoV due to abberation effects [16].

For the purposes of MAM, PSF photometry is not possible with a realistic amount of effort. The reason is the following: We are doing absolute photometry in special

[10] Atmospheric seeing describes, how much turbulence there is in the air. Good seeing means the atmospere is very calm and this will result in a higher angular resolution.

[11] An important property of the Gaussian is its Full Width Half Maximum (FWHM), which corresponds to the width of the Gaussian at half the maximum intensity. It is equal to $2\sqrt{2\ln(2)}$ times the width σ. Inside of an aperture radius of 3 times the FWHM ($\approx 7\sigma$) essentially 100 % of the starlight is included [17].

circumstances. Only integrating over the well known central part of the PSF does not work for absolute photometry because no total flux can be extrapolated from there. We do not know how much of the starlight is hidden in the flanks of the star, therefore we would not be able to tell which percentage of the total flux we calculated. The complete PSF curve is needed to get an absolute flux by integrating over it, but this is virtually impossible. Even if we could determine a complete model of the PSF for different focus positions and different positions in the field of view (FoV) the faint flanks would not be accurate enough. The reason is that there is always some fluctuation of the background brightness that will overpower the signal of the PSF wings [33]. Additionally MAM needs to observe and measure at large zenith angles, with higher airmass values. It is known that the image of objects approaching the horizon is deformed to elliptical shape by the increasing airmass. A changing PSF shape can lead to big changes in the flux determination. Therefore another method was chosen, which is aperture photometry.

3.6 Aperture photometry and growing curves

Absolute photometry with MAM was done using aperture photometry with a growing curve correction. This correction will be called the growing curve correction throughout the thesis, because it uses a growing curve, but typically when talking about growing curve correction a slightly different action is meant [15, 17, 32]. This technique is independent of the PSF shape and therefore more practical if the PSF is not well known. Essentially a circular aperture of a certain radius is defined, centered on the point source and all the counts inside are summed up to get the total count. To correct for the contribution of the background two larger apertures are defined, which form an annulus around the inner aperture. The region inside of the annulus is used for the background estimation (see Figure 13).

The total flux of the star is calculated as follows:

$$S = F - n_{\mathrm{pix}} N_{\mathrm{s}}. \tag{25}$$

S is the total electron count of the star, n_{pix} the number of pixels included inside the aperture, N_{s} the total number of background sky electrons per pixel (obtained by taking the mean of the annulus total count), and F the total electron count inside of the inner aperture.

Proper aperture photometry can only be done if the FoV is not too crowded with stars (otherwise there is no space left for background estimation, see section 4.2.3). Its success also relies on a non-curved brightness profile of the background, because this cannot be removed as easily as a brightness gradient. There is another analysis step needed to

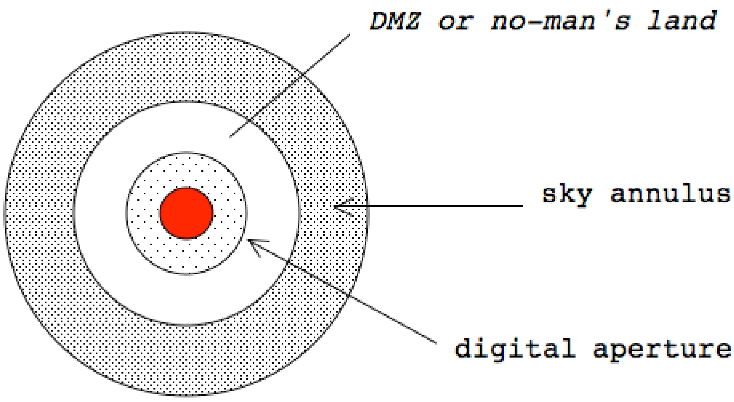

Figure 13: Aperture photometry on a point source (the red dot, in reality smeared by a PSF) is shown. The inner aperture is used to sum up all counts of the star. However it also contains counts originating from the background brightness, therefore another aperture annulus for background estimation is defined around the center (shaded area). Typically this annulus does not directly come after the inner aperture, but leaves out a small region to ensure that no star light is included in the background estimation. The total counts from the star can be calculated as in Equation 25. Image taken from [17].

ensure a proper background estimation, the growing curve correction.

In theory, plotting the total flux of a star inside an aperture against the aperture radius (after a preliminary background subtraction) will give curves that are growing as long as not all the starlight is inside and then stabilizing at some flux value. In reality, the preliminary background estimation will often not match with the real background. If this happens the curve will not stabilize, but either continues to grow or falls down again after a peak, meaning that the background was under- or overestimated. To ensure a correct background estimation this part of the analysis will be done by hand, selecting an interval for the background estimation for each star seperately. More details on the actual application of the growing curve correction can be found in section 4.2.3.

3.7 A concept for photometric measurements with MAM

Summarizing this chapter, I explain which is the approach for photometric measurements chosen for the MAM telescope, both in the frame of the Bachelor thesis and the realization of photometric measurements in the future. The MAM telescope is meant to measure the transmission of the atmosphere in the pointing direction of MAGIC, possibly in real time. The suitable kind of photometry to do in this case is absolute photometry. It requires knowledge of the magnitude of a star at airmass zero. There are several possibilities to determine the quantity:

1. Extrapolate the magnitude of a star at AM zero every night by observing it at different zenith angles and fitting the datapoints as in Equation 12. The real time measurement is not possible in this case.
2. Create a catalog of targets with the MAM, from stars next to gamma-ray sources. This is a work of many years[12]. However it has the advantage, that we do not need to know the relation between individual photometric systems and can avoid possible sources for systematic uncertainties arising from this transformation. The catalog would provide internally consistent reference data. This may be considered later but goes beyond this Bachelor thesis.
3. Use an existing catalog and calibrate the MAM system with respect to it. If the transformation relation between our photometric system and the catalogs system can be derived with enough precision it will enable the conversion of catalog star magnitudes to the MAM observational system.

The last of the three approaches was attempted in this Bachelor thesis. Finding a catalog that fulfills special requirements was not as easy as expected. Requirements for the catalog are:

- Enough non-variable stars (some hundreds)
- Uniform distribution over the sky of La Palma (down to $-60\,^{\circ}$ declination)
- Information on filter-dependent magnitudes and color indices
- Approximate completeness

I looked up a lot of different star catalogs and compared them according to the criteria listed above. There were none that fulfilled all the requirements, so I chose the most reliable and complete one, which is the Landolt catalog [23, 25, 27]. It is not suited for the long-term plans of MAM because Landolt observed only stars around the celestial equator (see Figure 14) but MAGIC also observes many extragalactic sources.

This thesis will provide an evaluation of the possibilities to fulfill the task of MAM (see section 2.1) with the chosen approach, i. e., by calibrating our system with respect to the Landolt standard photometric system.

[12] Only including VLZA observations in the catalog would be possible in considerably less time. This could be a starting point, from where observations by MAM could be increased successively towards full operation during all MAGIC observations.

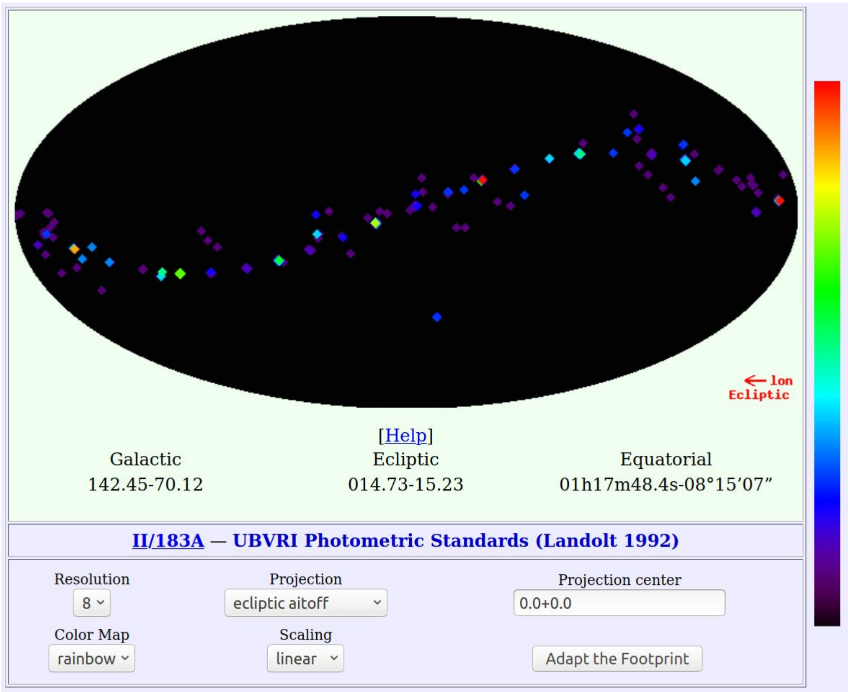

Figure 14: Distribution of Landolt standard star fields around the celestial equator. Ecliptic longitude runs along the long axis of the ellipse, representing the night sky. Each dot represents a standard star field defined by Landolt. One of them contains between 1 and up to more than 50 standard stars. The colors indicate how many stars are situated in the field. Red star fields for example contain a maximum of standard stars. Image taken from [42].

4 Photometric calibration of the Baader filter system

4.1 Calibration measurement

The calibration measurement was done in the night of 8th/9th November 2020. There were no clouds to be seen on the allsky camera (see section 1.2), neither high in the sky nor close to the horizon. Transmission values from LIDAR in Figure 15 confirm good conditions. Note that LIDAR measured the transmission in different directions close to the MAGIC targets throughout the night. This means it was often not pointing in the same direction as MAM. LIDAR measures the transmission at 9km, not through the entire atmosphere layer. Because of that LIDAR transmission values might not perfectly match the conditions in pointing direction of MAM. There were also measurements from the same night taken by the FRAM telescope (CTA) and the ARCADE Raman LIDAR. The three of them agree on the fact that there were no clouds for the whole night. While FRAM measured a VAOD between 0.05 and 0.07, ARCADE values are below 0.04[13]. The typical value for a very good night on La Palma is around 0.02[14], so results of the FRAM indicate no perfect transmission. On the whole this means that weather conditions were good but not extremely good for the entire night. Mean wind speed and gusts stayed at a value of 15 km/h, which was good because there are some doubts about the stability of the MAM telescope with stronger wind. The moon rose at 01:07 UT, but the stars that were imaged were all more than 30° away from it. There is no brightness gradient in the data, only a uniform brigthening of the background level can be seen.

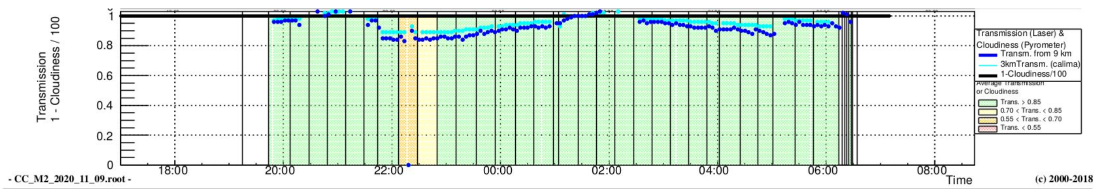

Figure 15: Atmospheric transmission at 9 km from the ground (dark blue datapoints) on 8th/9th November 2020. Transmission is plotted against UT time. Transmission values stay above 0.8 for the whole night and above 0.9 for most of the night. Plot taken from [29].

The data taking was accomplished with the existing control software of the MAM telescope[15] and a script that I wrote and tested for this purpose (make_cal.py [14]). The

[13]The data was communicated personally [35, 34]. For explanations of terms see section 3.2.3.

[14]See [8] but note that a significant discrepancy is reported between the FRAM VAOD measurements and higher ARCADE values, which is not yet understood.

[15]For further information about the control software the preceding Master's thesis can be consulted [13].

script uses basic functionalities that were already implemented, e. g., the control of the telescope devices like the mount, dome and camera, as well as new functionalities, that were written as a part of this Bachelor thesis. Two new features will be mentioned here:

1. To make the application of this script flexible for different dates I implemented a function that selects five stars for the calibration from the Landolt catalog [25], depending on their rise and set times and the total visibility timespan during the given night. Additionally, the function chooses only the brightest stars (brighter than 11 mag), in order to achieve a big enough signal-to-noise ratio (SNR) with a telescope aperture of only 5 inch, and the selection is composed from a wide range of color indices. The latter leads to a more precise calculation of the color transformation factors and applicability to different colored stars (see section 3.1).

2. For photometry it has to be assured that the target object does not saturate on the sensor, like described in section 2.2. This is done with a series of iterated images of different exposure times, determining the maximum pixel count in the region of the star at every step. The function terminates if 25000 - 35000 counts out of a maximum of 65504 counts is reached[16]. In reality, the counts were sometimes a bit lower or higher but they all stayed between 20000 - 40000 counts, which is fine for doing photometry (see section 2.2).

Alltogether this enabled a nearly complete automatic mode of operation during the measurement. Before starting the observation, 20 dome flats were taken for each of the filters. The measuring process was realized as a loop containing several steps:

1. Repositioning of the MAM telescope

2. Centering the star in the secondary camera

3. Using the auto-exposure function to capture an image with every filter

The outcomes are 181 images of the five stars SA 92-312, SA 96 36, SA 97 284, SA 99 438 and SA 115 271. The target objects are imaged in the four different filters of the Baader filter system (see section 2.2) and each of the star-filter combinations covers a wide range of zenith angles from 28° to about 80°.

[16]The acceptance interval was implemented to be a bit smaller than the actual range that allows useful data. This was done to ensure that images stay in the linear region.

4.2 Analysis of the calibration measurement

For the analysis of the data I wrote another python module (analyze_cal.py [14]). Since a part of it, namely the growing curve correction, had to be done by hand[17], the code consists of seperate functions that were applied one after the other. Starting with selection of good quality data, the following parts describe how the analysis was done.

4.2.1 Selection of good quality data

The first step was to look through all images one by one. Resulting from this check, 24 were excluded from the analysis since they contained some disturbance that would have lead to wrong results.

Figure 16 and Figure 17 show the two kind of defects that can be found among the bad images. The effect in Figure 16a (and also in Figure 16b) was most propably caused by a part of the camera tower structure of MAGIC 1 or possibly by a part of the telescope itself obstructing the view. It always happened when the telescope was pointing to the southeast at high zenith angles. As mentioned in section 2, the MAM telescope is situated inside of the fenced area of MAGIC 1, to the northwest of the telescope and the tower structure, so the explanation is quite plausible. An even more detailed reconstruction of the problem can be provided by looking at Figure 16b. The brightest stars on it have strong spikes, because of the diffraction effect of light passing at the edge of some object. Since the spikes are known to always emerge perpendicular to this edge, the object in the Field of View (FoV) had an edge that goes diagonally from the upper left to the lower right corner.

Approximately the other half of the bad images did not pass the selection criteria because of elongated stars. There was a curious pattern for the occurence of the problem: It always happened when the telescope was pointing to a zenith distance of $(30 \pm 2)\,^\circ$. The observed stars are all situated around the celestial equator. Therefore a possible explanation could be that for a pointing of $30\,^\circ$ zenith distance towards the equator, the telescope is always in a certain position where it gets stuck. Then the tracking is blocked for some moments and the stars become trails on the image. Knowing the setup and where possible obstacles inside the dome could be, the above explanation is likely. The smeared images only happened for three of the stars. This was not further investigated.

Once only the images of good quality were selected, data reduction could be performed.

[17] For now, because the system is not automated yet.

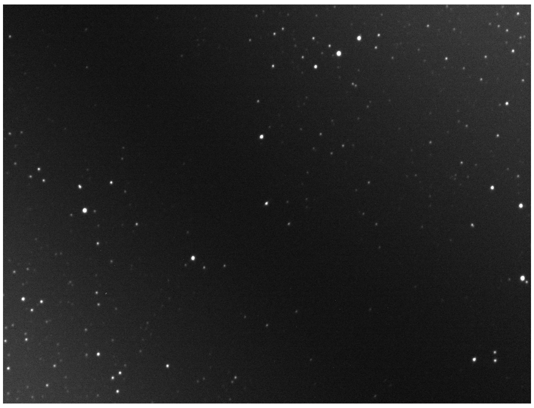

(a) An object in the line of sight causes a shadow

(b) Diffraction produces spikes around the stars

Figure 16: Images taken by the MAM telescope during the calibration measurement. An object in the FoV produces shadows and spikes. Probably MAM was pointing to a part of the camera tower of MAGIC 1 or to the telescope itself. Affected images were excluded from the analysis.

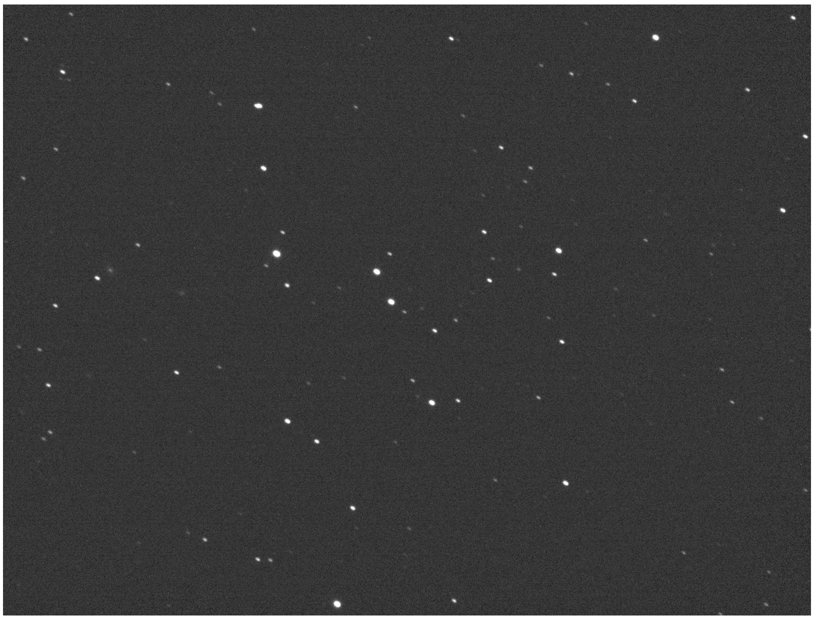

Figure 17: Image taken by the MAM telescope during the calibration measurement. The frame shows elongated stars and was taken at approximately 30° zenith angle. This kind of defect in the images did always happen when pointing to the mentioned zenith angle. A possible explanation would be an obstacle in the way of the telescope movement, stopping the tracking for some moments. The affected images were excluded from the analysis.

4.2.2 Data reduction

As described before, the images have to be cleaned before performing further analysis steps. A basic cleaning was chosen, including only the subtraction of master dark frames and a flat-field correction (see 3.4). Although this led to a moderate cleaning effect, especially on the edges of the image, it was good enough for the purpose of aperture photometry in the clean center region of the frame.

For all light and flat frames, a master dark frame was produced from an interpolation of averaged dark frames, matching the exposure time of the treated image. Making a series of different exposures for a chip temperature of $-15\,°\mathrm{C}$, the dark current of each pixel was fitted seperately (dark.py [14]). The fit values were stored in two new FITS files and were retrieved when a dark field for a given exposure time was needed. The quality of the interpolated master dark frames is not optimal because a lot of hot pixels remain in the reduced images, compare Figure 18a and 18b. I also tried applying a real averaged dark frame to the same image, which was a shot of 120s exposure time from a test run. The result can be seen in Figure 18c. The so calibrated image contained less hot pixels but they could not be removed completely. The reason for this is not clear to me because my expectation was that even though the combined images were not taken at the exact same time, they should match. Typically the camera should reproduce the conditions under which an exposure is done by cooling the sensor to $-15°\mathrm{C}$, so the dark current should be the same every time.

In the end the interpolated master dark frames were applied to the data. It was the only feasible way to treat a set of images with a wide range of exposure times without having to capture at least 10 dark images for every exposure time. Apart from that, the taking of real dark frames was not remotely possible with the installed system: The camera does not have a shutter that can be closed from remote and it is not sufficient to close the dome. There are still some small lights from devices blinking inside the dome that cannot be switched off.

A classical approach for the flat-fielding was chosen, which is to compute an average image from several raw images. This was repeated for each filter. Before combining the raw files, they were treated with master dark frames in order to remove the hot pixels and bias level (3.4).

Figure 19 shows example images of SA 92-312 in raw state (19a) and after data reduction (19b). In spite of the cleaning there remain a few hints of dark spots, caused by dust on the mirror or more likely on the glass plate in front of the sensor. The two bright regions[18] at the right border of Figure 19a are removed in Figure 19b, due to the dark subtraction.

[18]This effect is called amplifier glow (or amp glow). It is caused by circuits of the readout electronics close to the sensor, which transfer heat to the sensor and produce a higher dark noise.

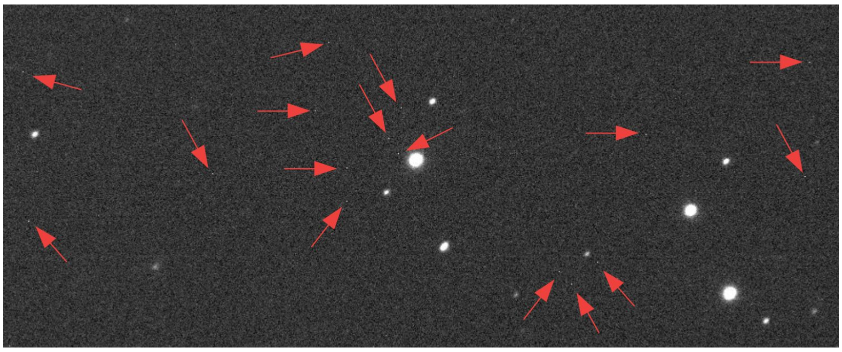

(a) Cutout from the untreated image. A lot of hot pixels can be seen, in spite of a chip temperature of −15°C. This is due to the long exposure time of 120 s.

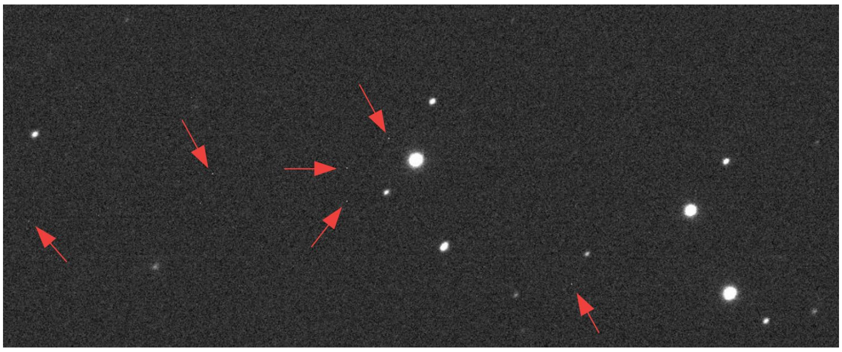

(b) Cutout from the image that was treated with the interpolated master dark frame. Contains visibly less hot pixels but some remain.

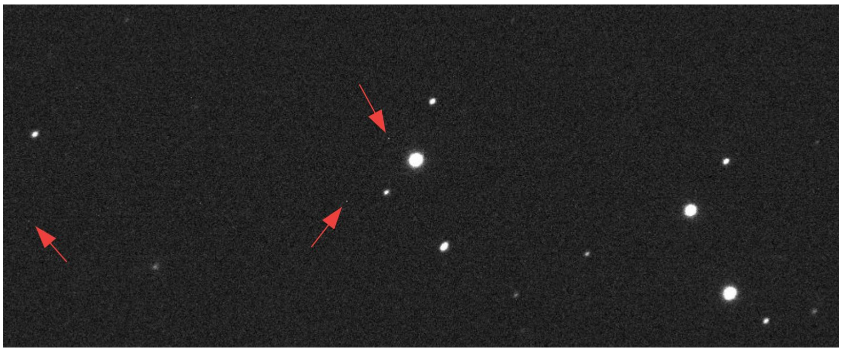

(c) Cutout from the image that was treated with the real averaged dark frame. Even then there remain some hot pixels. It was not further investigated why that is the case.

Figure 18: Comparison of data reduction quality with real and interpolated darks. Each of the red arrows points out a hot pixel.

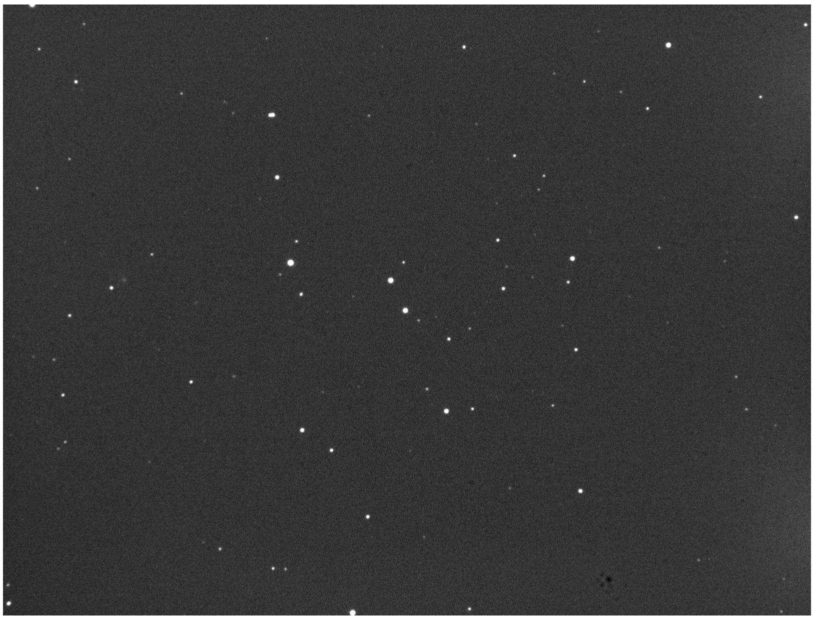

(a) Raw image containing all sorts of contaminations, e. g., dark spots from dust at the bottom border and two diffuse bright areas at the right border. The image also contains hot pixels and vignetting but they are not well visible on a single shot image.

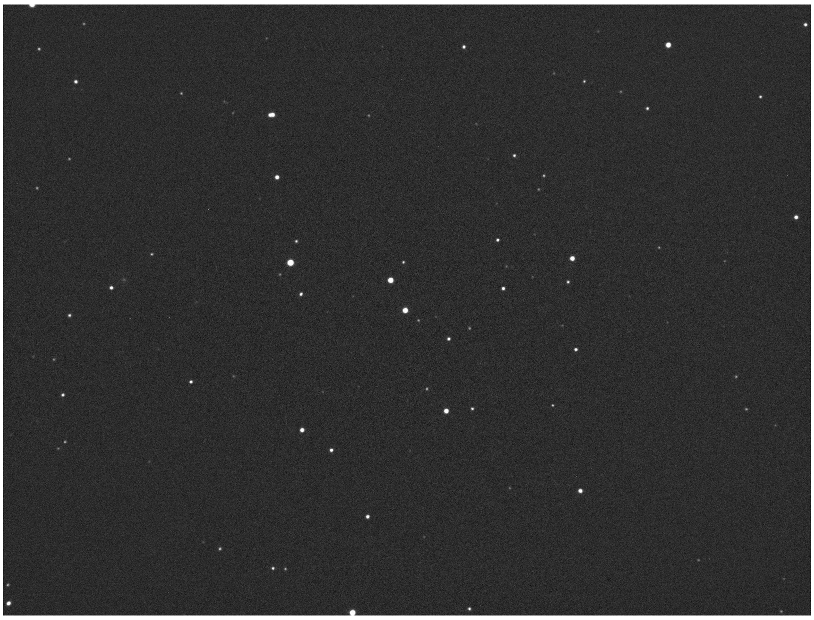

(b) Reduced image, clean except for some remaining hints of dust.

Figure 19: Comparison of image data before and after data reduction. Most of the defects could be removed by a basic treating with averaged dark and flat frames.

To avoid most of the remaining defects mentioned in this section, the region of interest around each star was carefully inspected for hot pixels. Additionally, the area used for background estimation was chosen to be as close as possible to the star and as narrow as possible, still sampling enough pixels for a good averaging effect. This is described in more detail in the following section.

4.2.3 Aperture photometry with growing curve correction

The aperture photometry was done using the first version of a python program by Arno Riffeser [38], which displays a FITS image and offers different options. For instance a Gaussian or a Moffat curve could be fitted to a star (see section 3.5 on PSF photometry), but the relevant option here is the growing curve plot. The program plots a first growing curve with default start parameters for the apertures. In most of the cases this first automatic background estimation was found to underestimate the background brightness, i. e., the curve did not converge to a stable level but continued to grow slowly like in Figure 20. This is corrected by the user, who by sense of proportion selects an interval that will be considered as the new background and to which a parabola will be fitted. The contribution of the background to the brightess increases with the aperture radius squared, that is why it has to be a parabolic fit. The output of the program is a table with the pixel positions of the selected spot, the total pixel counts of the star that result from the subtraction of the chosen background and a corresponding uncertainty, the mean sky brightness per pixel and the interval limits.

The uncertainty for the total count of a star was calculated with:

$$\sigma = \sqrt{F}. \tag{26}$$

F is the total count inside of the inner aperture (all the starlight plus all the photons coming from the sky in the contained area). It is correct to directly take the square root of the number of counts because I used a gain of $1\,e^-/\mathrm{ADU}$ (see section 3.3), which means the number of counts corresponds to the number of electrons generated. In section 3.4 the combined noise/uncertainty was introduced. The two last terms under the square in Equation 22 were the dark noise and the read noise of the camera sensor. For my measurement they are totally dominated by the photon (electron) noise from the star and the background. Total photon (electron) counts from the measurement lie between half a million and more than ten million. The read noise is $\approx 1.6\,e^-\mathrm{rms}$[19] at a gain of $1\,e^-/\mathrm{ADU}$ (see technical specifications of camera in appendix B) and the dark noise is around $2.0\,e^-\mathrm{rms}$ (for a maximum exposure time of 120 s, given a chip temperature of

[19]The read noise or other noise components are sometimes written in units of $e^-\mathrm{rms}$. RMS/rms stands for Root Mean Square.

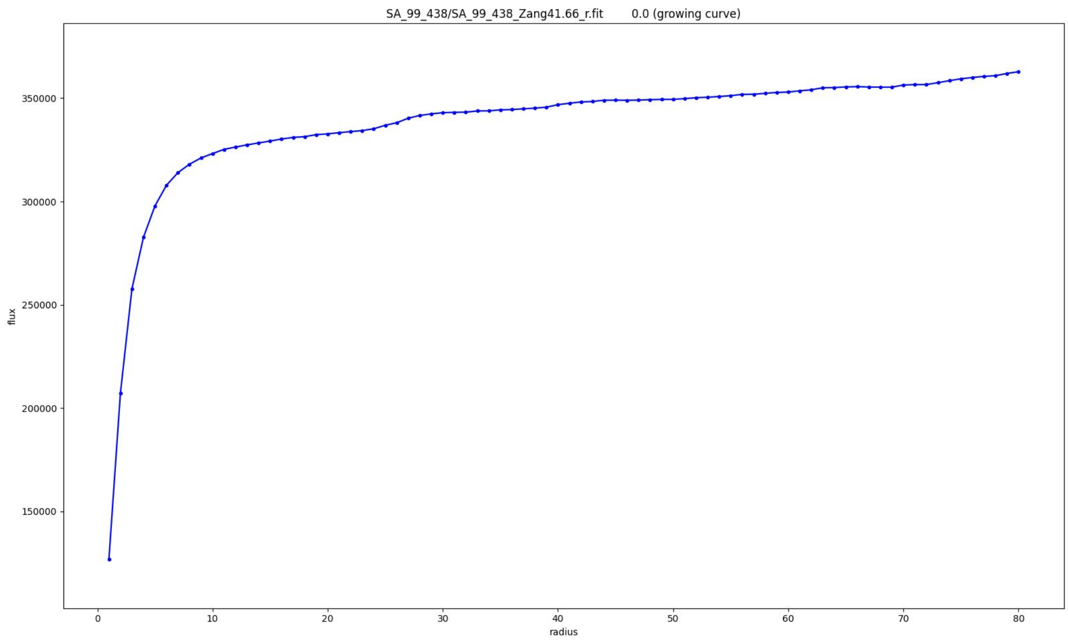

Figure 20: Growing curve after the preliminary automatic background estimation. Plot of total count of Analog-to-Digital Units (ADUs) detected inside an aperture (called flux) against the aperture radius. A good background estimation is indicated by a growing curve converging to a constant value. This plot shows a growing curve resulting from an underestimated background brightness.

$-15°$C and assuming a dark current value of $0.01\,e^-/\mathrm{s}$[20]). The contribution of the read noise and dark noise components to the overall noise were therefore neglected.

With the above formula I got quite small uncertainties in the results, however it only takes into account statistical effects. The systematic effects should be expected to be quite big. They can result from changing interval limits and the fact that the growing curve is displayed at a certain scale, hiding details to the eye of the user. In this way a faint star might be overseen in the curve and included in the background estimation. The centering of the aperture on the star should not have a major influence on the result. When selecting a star the program makes a 2D Gaussian fit to determine the exact center. This means the manual centering only needs to have a precision of 2-3 pixels.

[20] I want to stress that this is just a rough estimate, but the order of magnitude is largely enough here, considering the extremely high count values. For the estimate I used values from an analysis of another ASI1600mm camera [39] with the exact same model as the one used for MAM.

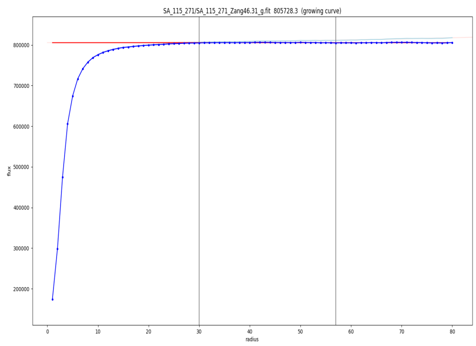

(a) SA 115 271 at 46 ° ZD in filter g

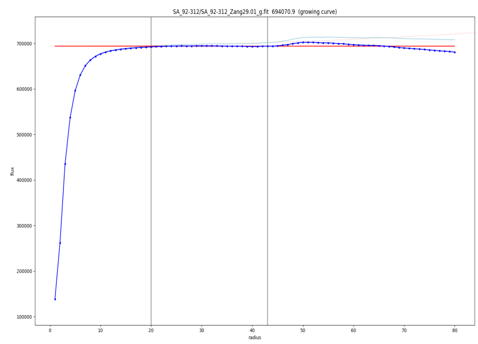

(b) SA 92-312 at 29 ° ZD in filter g

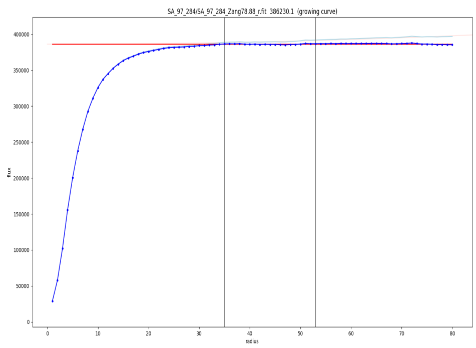

(c) SA 97 284 at 79 ° ZD in filter r

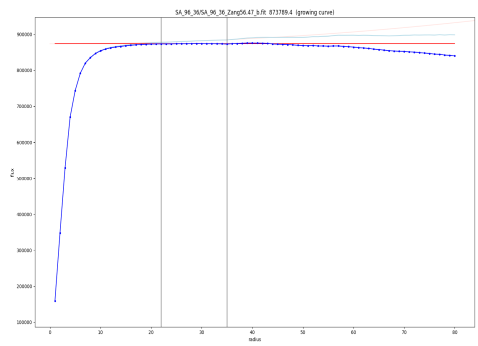

(d) SA 96 36 at 56 ° ZD in filter b

Figure 21: Growing curves from the analysis: Plot of total count of Analog-to-Digital Units (ADUs) detected inside an aperture (called flux) against the aperture radius. The two gray lines mark the limits of the chosen interval for background estimation. The corresponding growing curve, resulting from the subtraction of the new background is plotted in blue. The red horizontal line points to the total count included inside the aperture, which corresponds to the total count of the star if the background estimation is of good quality.

In Figure 21 some examples of growing curves from the analysis are shown. Not all were included since there is one for each good quality image, leading to a total of nearly 160 growing curve plots. The growing curves are of different shape and sometimes have additional wobbles at big apertures. A shallow slope like in Figure 21c indicates that the image was taken at high zenith angle, because the total light of the star gets distributed over a larger region due to atmospheric light scattering. The small wobbles are caused by faint stars close to the target. The interval for the background estimation in such cases was settled between the target star and neighbor stars, provided this was possible (see next paragraph). Growing curves 21b and 21d show a drop in the curve at high apertures. If the background estimation was correct and the background brightness in the image was perfectly uniform at the same time this could not happen. Probably it can be attributed to a slightly non-uniform background. I already suspected this from the reduced images because the vignetting (see section 3.4) was not entirely removed by the master flat frames. The mean background brightness from the center region around the star is slightly bigger than the mean background brightness further out. This means if the mean background from the center is subtracted from the outer regions it will produce negative pixel values. At some point the aperture starts including these negative values, adding them to the sum, reducing the total count. That is why the curve drops again after reaching a maximum. In this case it was important to keep using an interval close to the center for background estimation, to avoid underestimating the background. Another interesting detail can again be seen in growing curve 21c: The slope of the growing curve is sagging a bit in the beginning, meaning that the curve first increases in steepness before getting shallower. Hints of that can also be seen on two of the other curves (21a and 21b). This should not be the case for a perfectly focused camera, it indicates a slightly defocused camera. The amount of defocusing is no problem for the purpose of this work or photometry in general, therefore it will not be discussed further.

For the stars SA 92-312, SA 96 36, SA 97 284, and SA 115 271 the growing curve method worked out fine, but not for the remaining star SA 99 438. The first and most direct approach failed, because its position is halfway into the milky way band in the sky, leading to a crowded image. There was a neighbor star of the target star, which made it impossible to do a proper background estimation since there was not enough space left to estimate the background. In pixel coordinates the center positions of the stars were only about 25 pixels away from each other. I first considered measuring both stars together in one aperture in the first step. The second step would have been to measure the close-by star seperately (also with the growing curve program) and then subtract the values to get the total count of the target star. But this basically would have meant reproducing the exact same problem reversed and in a more complicated way. Another idea was to simply ignore the pixels of the neighbor star for the growing curve evaluation. Arno Riffeser therefore implemented a new option in the program, which is the masking of pixels. This way a region could be excluded from the evaluation by the growing curve. In Figure 22 this special approach for SA 99 438 is shown, blue pixels designating masked pixels. After placing the mask, the growing curve method

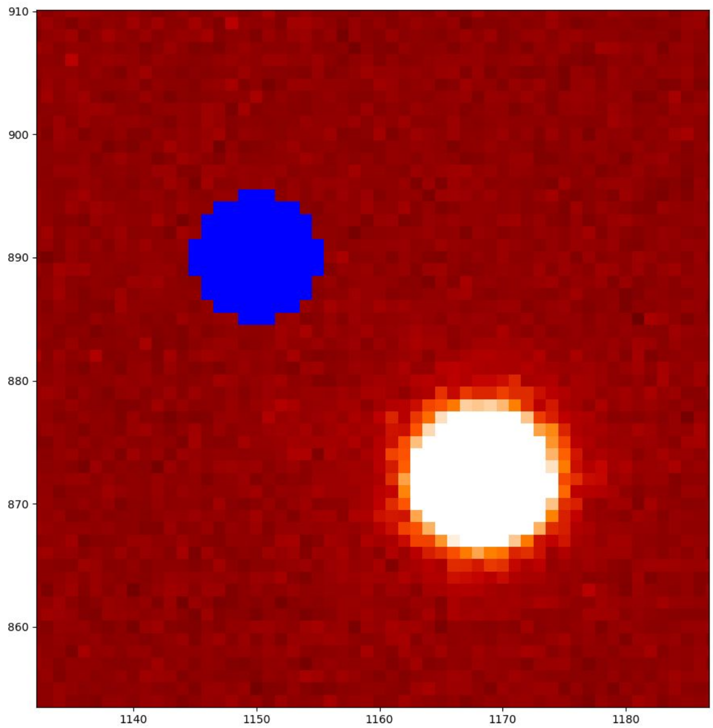

Figure 22: SA 99 438 and a close neighbor star in the growing curve program, which has been masked with blue pixels.

could be applied as described before, blue pixels were ignored. Note that this approach can increase the uncertainties since we do not know for sure if the PSF of both stars slightly overlap or not.

4.2.4 Extrapolation of airmass zero

For every star-filter combination, the counts were converted to flux values by normalizing with the exposure time of the picture in question, and then to instrumental magnitudes using Equation 10 from section 3.3. The returned uncertainties from the growing curve program were treated with Gaussian error propagation to get error values for the magnitudes. Fitting the datasets, following Equation 12, yields the extrapolated instrumental magnitude $m_{\mathrm{instr},0}$ of a star at airmass (AM) zero and the extinction coefficient κ in a certain filter. The size of the datasets for different stars and filters varies between 6 and 11. In four cases the results were refitted and replotted, excluding one of the datapoints. These are corresponding to four images that passed the test of good quality,

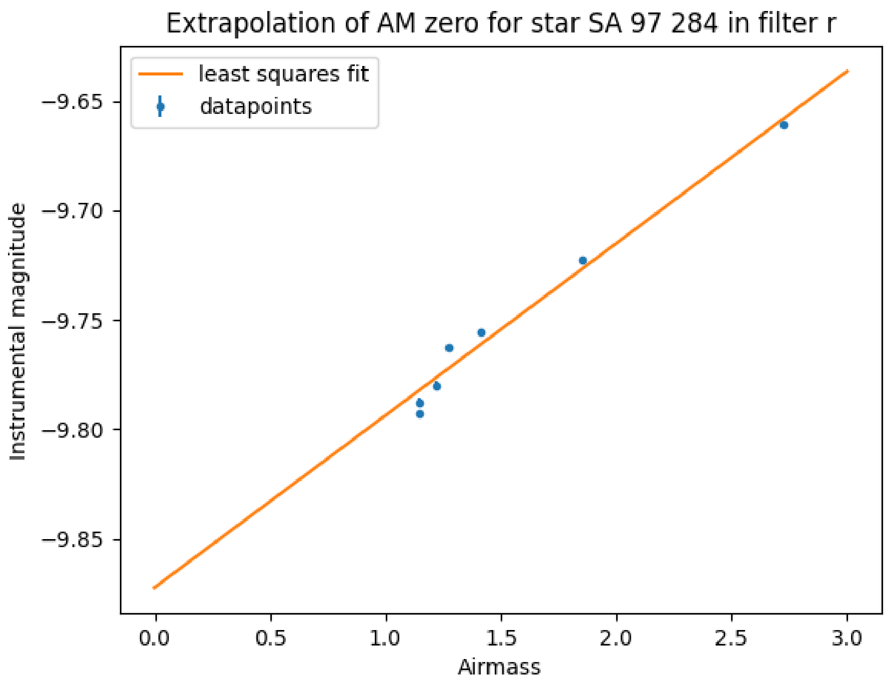

Figure 23: Extrapolation of AM zero for star SA 97 284 (filter r). Plot of instrumental magnitude against airmass, containing the datapoints taken at different zenith angles in blue and the least squares fit in orange.

but only barely. From looking at the images I could not definitely say if there was a major disturbance, so I decided not to exclude them completely but to investigate both cases (with and without the four datapoints). Figure 23 shows an example of an airmass plot for star SA 97 284 in filter r. For the rest of these plots see appendix A.1, there are 20 in total. The result values of instrumental magnitude at airmass zero $m_{\mathrm{instr},0}$ with uncertainty σ_{m} and extinction coefficient κ with uncertainty σ_{κ} for all stars can be found in Tables 1-5. Tables 6-9 do not contain new values but display all extinction values and uncertainties for the same filter in one table to make the comparison more convenient.

Before discussing the results I would like to remind of three things: As mentioned in section 4.2.3, the calculated uncertainties only take into acount the statistical uncertainty and no systematic errors. Furthermore, by fitting datapoints with different recording times and airmasses together, it was assumed that the extinction is both constant over time and all over the sky. This was considered a valid approximation for the purpose of the measurement but is not the case in reality (see section 3.2). And finally and most importantly, extinction has a color dependent term. Strictly speaking, the expectation for the extinction coefficients measured with different stars is not that they are the same, but that they differ slighty for filters r, g and b and more significantly for filter l.

SA 92-312					
filter	κ	σ_κ	$m_{\text{instr},0}$	σ_{m}	excluded datapoint #
l	0.118	0.005	-10.913	0.012	
l	0.149	0.007	-10.962	0.012	11
r	0.088	0.004	-10.186	0.012	
g	0.136	0.007	-9.549	0.015	
g	0.161	0.009	-9.587	0.014	10
b	0.176	0.012	-9.226	0.022	
b	0.207	0.010	-9.273	0.017	9

Table 1: Result values of extinction κ and instrumental magnitude $m_{\text{instr},0}$ for SA 92-312

SA 96 36					
filter	κ	σ_κ	$m_{\text{instr},0}$	σ_{m}	excluded datapoint #
l	0.160	0.017	-11.041	0.023	
r	0.086	0.023	-9.451	0.032	
g	0.180	0.004	-9.829	0.008	
g	0.146	0.015	-9.782	0.020	10
b	0.212	0.010	-10.308	0.021	

Table 2: Result values of extinction κ and instrumental magnitude $m_{\text{instr},0}$ for SA 96 36

SA 97 284					
filter	κ	σ_κ	$m_{\text{instr},0}$	σ_{m}	excluded datapoint #
l	0.123	0.007	-10.712	0.010	
r	0.079	0.005	-9.872	0.009	
g	0.166	0.012	-9.428	0.016	
b	0.226	0.017	-9.274	0.023	

Table 3: Result values of extinction κ and instrumental magnitude $m_{\text{instr},0}$ for SA 97 284

SA 99 438					
filter	κ	σ_κ	$m_{\mathrm{instr},0}$	σ_{m}	excluded datapoint #
l	0.209	0.004	−12.434	0.005	
r	0.111	0.006	−10.506	0.009	
g	0.162	0.006	−11.080	0.008	
b	0.252	0.004	−11.875	0.007	

Table 4: Result values of extinction κ and instrumental magnitude $m_{\mathrm{instr},0}$ for SA 99 438

SA 115 271					
filter	κ	σ_κ	$m_{\mathrm{instr},0}$	σ_{m}	excluded datapoint #
l	0.176	0.006	−11.929	0.009	
r	0.116	0.005	−10.640	0.007	
g	0.168	0.004	−10.672	0.006	
b	0.231	0.005	−10.966	0.009	

Table 5: Result values of extinction κ and instrumental magnitude $m_{\mathrm{instr},0}$ for SA 115 271

Filter l extinction coefficients			
Star ID	κ	σ_κ	excluded datapoint #
SA 92-312	0.118	0.005	
SA 92-312	0.149	0.007	11
SA 96 36	0.160	0.017	
SA 97 284	0.123	0.007	
SA 99 438	0.209	0.004	
SA 115 271	0.176	0.006	

Table 6: All result values of extinction κ for filter l

Filter r extinction coefficients			
Star ID	κ	σ_κ	excluded datapoint #
SA 92-312	0.088	0.004	
SA 96 36	0.086	0.023	
SA 97 284	0.079	0.005	
SA 99 438	0.111	0.006	
SA 115 271	0.116	0.005	

Table 7: All result values of extinction κ for filter r

Filter g extinction coefficients			
Star ID	κ	σ_κ	excluded datapoint #
SA 92-312	0.136	0.007	
SA 92-312	0.161	0.009	10
SA 96 36	0.180	0.004	
SA 96 36	0.146	0.015	10
SA 97 284	0.166	0.012	
SA 99 438	0.162	0.006	
SA 115 271	0.168	0.004	

Table 8: All result values of extinction κ for filter g

Filter b extinction coefficients			
Star ID	κ	σ_κ	excluded datapoint #
SA 92-312	0.176	0.012	
SA 92-312	0.207	0.010	9
SA 96 36	0.212	0.010	
SA 97 284	0.226	0.017	
SA 99 438	0.252	0.004	
SA 115 271	0.231	0.005	

Table 9: All result values of extinction κ for filter b

This complicates the evaluation of the results since it will not be clear to which effect a deviation has to be attributed, to uncertainties and lack of precision in the measurement or to the color dependence.

In the following κ_{l}, κ_{r}, κ_{g}, κ_{b} will denote the extinction coefficients for filters l, r, g, b, respectively. $\overline{\kappa_{\mathrm{r}}}$, $\overline{\kappa_{\mathrm{g}}}$, $\overline{\kappa_{\mathrm{b}}}$ will denote the mean extinction values for filters r, g, b, respectively. From the tables and plots several conclusions can be made, see next paragraphs[21].

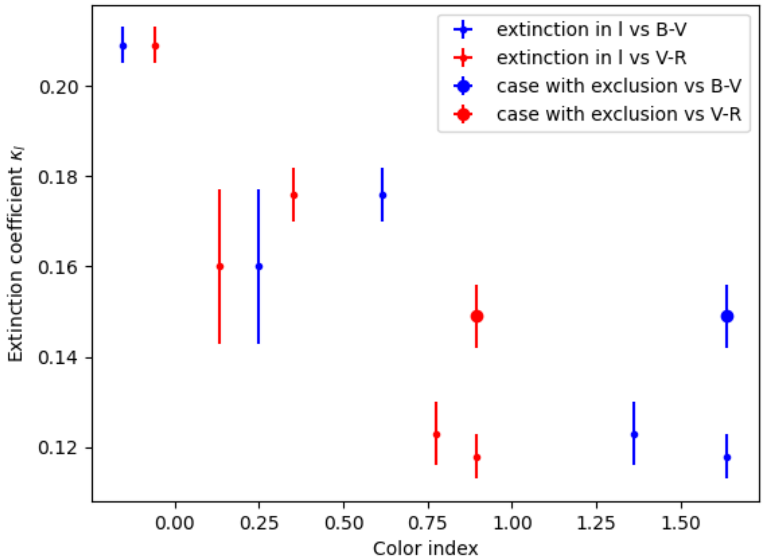

Figure 24: Atmospheric extinction values for the l filter depending on the color index of a star. Plot of extinction coefficients against the color indices $(B-V)$ and $(V-R)$ of the stars. The expectation is a higher extinction value for bluer stars (for smaller color indices). The sample of five stars is too small to confirm a direct correlation between color and extinction, but it can be suspected.

The uncertainties for extinction and magnitudes are very small. This is not realistic when taking into account the systematic effects.

The results for the extinction determined from a single star dataset for the filters r, g and b are consistent among themselves, since the extinction increases with decreasing central wavelength of the applied filter. The extinc-

[21]Explanations from section 3.2 are relevant and will be used without further reference in the following paragraphs.

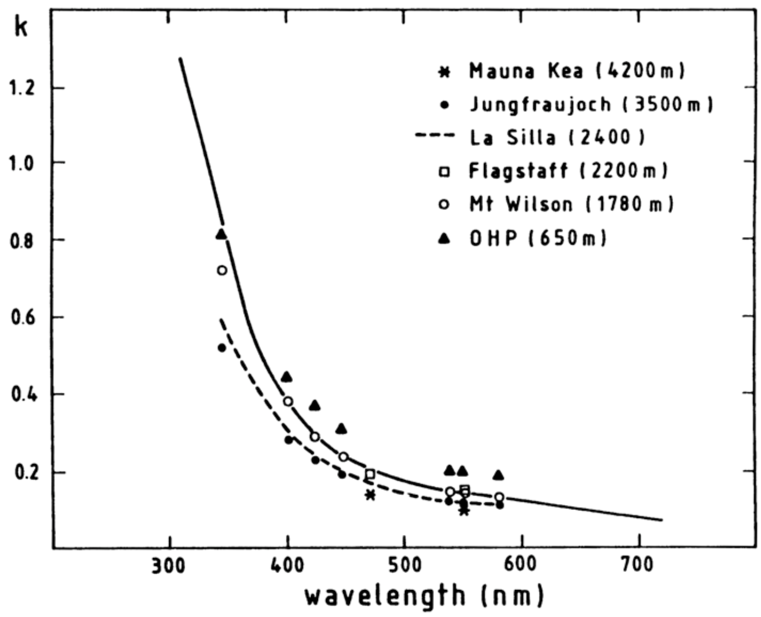

Figure 25: Atmospheric extinction for different astronomical observatories and altitudes. Plot of extinction coefficient κ against wavelength of light in nm. Measurements from different altitudes above sea level are shown. The extinction decreases with the height of the observing site, because a part of earth's atmosphere is left behind. Graph taken from [17].

tion coefficient calculated from the l filter data is always somewhere in between the other three values, which makes sense on a very rough scale but details are discussed in the next point.

Extinction in l filter (Table 6): The values are quite scattered, ranging from $\kappa_l = 0.118$ to $\kappa_l = 0.209$. Single error intervals do not overlap in most cases, triple intervals only in a few. This significant difference can be explained by the color dependent term of extinction, which becomes especially relevant for broad passbands like the l band, ranging from about 400 nm to 700 nm (see Figure 4). The total light of a red star will experience less extinction than of a blue star when passing through the atmosphere. The l filter does not block components of the visible spectrum, so the extinction value will vary depending on the observed star. The expectation is that the coefficient is smaller for redder stars. To check if my data is precise enough to show this direct correlation between the color indices and the results for the extinction in l band, I produced the plot which is shown in Figure 24. The correlation is not strong enough to confirm the above explained because of wide scattering but a tendency towards higher l extinction values for bluer stars can be suspected. More precision and a bigger sample of stars would be needed to show that relation. Figure 25 shows measurements of extinction at different observing sites and altitudes. Because of the wide passband, results in filter l cannot be well compared to the graph, except that the values are overall plausible for a wavelength range of 400 nm to 700 nm and an observing altitude of 2200m above sea level.

Extinction in r filter (Table 7), g filter (Table 8) and b filter (Table 9): Filter r shows a discrepancy among the extinction values calculated for different stars, but the spread of the scatter is smaller than for filter l. Single error intervals do not overlap in most cases, the triple error intervals overlap in many cases, but not all. The discrepancy cannot be attributed definitely to limited precision or to the color dependent term of extinction. The mean extinction value of $\overline{\kappa_\mathrm{r}} = 0.096$ matches the value read from Figure 25 for a central wavelength of 650 nm. For both filter g and b the interpretation is similar to filter r. The values mostly agree among themselves. Deviating measurements, especially the highest and lowest values, seem to be caused by the influence of one of the possibly falsified datapoints (like $\kappa_\mathrm{g} = 0.136$ and $\kappa_\mathrm{g} = 0.180$), but could also be a result of the color dependent part of extinction (like $\kappa_\mathrm{b} = 0.252$ for the bluest of the stars). The set of values for filter g actually looks a lot more consistent without the doubtful datapoints ($\kappa_\mathrm{g} = 0.161, 0.146, 0.166, 0.162, 0.168$). Apart from that, the mean extinction values $\overline{\kappa_\mathrm{g}} = 0.161$ and $\overline{\kappa_\mathrm{b}} = 0.226$[22] are plausible (compare Figure 25) for central wavelengths of 550 nm and 450 nm for filters g and b, repectively.

The instrumental magnitudes are offset from the real magnitudes by the zero point of the observational system. Therefore they cannot be compared directly to the catalog magnitudes of Landolt in Table 10. However the results pass basic consistency checks, e. g., the instrumental magnitude in the l filter is always the brightest one. This is expected since the transmission curve for filter l is broader than the three for the rgb filters. Another quantitative result, which is reflected in both, the value set from the Landolt catalog and the measurement, is the color of the stars. In Table 10 for instance it can be seen that SA 92-312 is brightest in the R filter and has a large color index of 1.638, meaning that it is a very red star. This is reflected in the measurement because in terms of magnitudes a value of $m_\mathrm{instr,0,r} = -10.186$ for filter r is brighter than $m_\mathrm{instr,0,g} = -9.587$ for filter g or $m_\mathrm{instr,0,b} = -9.273$ for filter b. The latter also holds for the comparison of measurement and catalog data of the other stars. For example SA 96 36 has a color index of $B - V = 0.247$ and is a 'more blue' star with $m_\mathrm{instr,0,r} < m_\mathrm{instr,0,g} < m_\mathrm{instr,0,b}$. This inequality equation at some point switches signs, when going through all the stars by color index.

About the four additional cases: The exclusions of one of the datapoints has more impact on extinction values than on the magnitudes it seems. Results for the extinction

[22]The values used for the mean are the ones excluding the doubtful datapoints.

coefficient, taking into account doubtful data, are in all cases found to produce the highest or lowest values compared to values from the same filter.

Related to the special analysis of star SA 99 438 (see section 4.2.3): A check of the values shows no significant difference to the other stars. In two cases of four (filter l and b) the values for extinction are a bit higher than the values from the other stars but that can very well be the normal scattering effect or a result from a dominant color dependent term, since SA 99 438 is the star with the smallest $(B - V)$ color index. Therefore I conclude that the PSF of SA 99 438 and neighboring star were not overlapping significantly and the masking was a successful way to deal with the crowded field.

Star ID	m_{R}	m_{V}	m_{B}	$B-V$	$V-R$
SA 92-312	9.701	10.595	12.233	1.638	0.894
SA 96 36	10.457	10.591	10.838	0.247	0.134
SA 97 284	10.014	10.788	12.151	1.363	0.774
SA 99 438	9.457	9.398	9.243	−0.155	−0.059
SA 115 271	9.342	9.695	10.31	0.615	0.353

Table 10: Star magnitudes and color indices from the Landolt catalog [25].

The conclusion from the discussion above has to be the following: The values for the extinction are all roughly confirming values from other measurements, but should be considered with caution. The reason is that there are many different effects influencing the real extinction at a certain place and time, in a certain wavelength and pointing direction[23]. They can not be taken into account all at the same time without highly increasing the complexity of the measurement and the analysis. They are therefore beyond the scope of this study. The results for the instrumental magnitudes are more satisfying in a way but cannot be crosschecked as well and have to be treated with caution because the weather conditions seem to have been good but not extremely good in the night of the measurement. Lastly there is a tendency to be seen concerning the four datapoints of doubtful quality: The results for the extinction coefficient including these were always off from the rest by a value between 0.01 and 0.03. They should be excluded from the analysis and will not be used in the last step. The last step will give results for the zero points and color terms of the photometric system and enable us to directly compare a measured intensity with an expected intensity of a star in future measurements.

[23]There are more effects that were not addressed in this chapter but mentioned in section 3.2.3, e. g., the seasonal variation of the extinction coefficient or the influence from Calima dust in the atmosphere of La Palma, which is not well known.

4.2.5 Calculation of zero point and color terms

The final step of the analysis was to determine a transformation relation between Landolts standard system and the MAM system. The first part of this subsection will only state the results with some remarks on striking elements. In the second part I will discuss them in more detail.

The classic magnitude transformation between photometric systems, as defined in Equation 14, was done with a χ^2-minimization. The result values for the zeropoints ZP and transformation coefficients a are listed in Table 11 with corresponding uncertainties.

filter	C	a	σ_{a}	ZP	σ_{ZP}
r	$V-R$	−0.091	0.012	19.977	0.007
	$R-I$	−0.106	0.012	19.984	0.007
g	$B-V$	−0.169	0.008	20.463	0.006
	$V-R$	−0.300	0.015	20.464	0.006
b	$U-B$	0.152	0.006	21.234	0.005
	$B-V$	0.219	0.008	21.145	0.006

Table 11: Final results for the application of χ^2-minimization to the linear case in Equation 14. Final results are for the color transformation coefficients a and the zero point ZP for filters r, g, and b and related color indices C. σ_{a} and σ_{ZP} are the corresponding uncertainties.

I also tried applying the quadratic χ^2-fitting, according to Equation 16 in section 3.3. The results for the calculated zero points ZP and color transformation coefficients a_1 (first order) and a_2 (second order) for filters r, g, and b are listed in Table 12 along with their uncertainties. On first sight there are at least two significant inconsistencies: For filter r, the values for the first order transformation coefficient $\sigma_{\mathrm{a},1}$ have changed completely compared to results for a from the linear fit. Furthermore the second order transformation coefficient $\sigma_{\mathrm{a},2}$ in the r filter is bigger than the linear coefficient. Neither does correspond to the expectation, because the quadratic term should only be a small correction [37]. For filters g and b these expectations are fulfilled, but the uncertainties for the second order transformation coefficients are quite big. Because of this I tried to reproduce the results by varying the input parameters, according to a Gaussian distribution. If the results from the randomly generated input are similar to the analytic solution, the solution is considered stable. I generated the Gaussian around the input parameter $m_{\mathrm{instr},0}$ with the uncertainty σ_{m} as standard deviation. Then I sampled random input values from this distribution and applied the fit procedure. This random draw and subsequent fitting was repeated 10.000 times for ever filter-color combination.

From the 10.000 resulting fit values I computed the means and the standard deviations of a_1, a_2, and ZP. They can be found in Table 13 and seem to confirm the result values and uncertainties from the analytic solution. This will be discussed below.

filter	C	a_1	$\sigma_{\mathrm{a},1}$	a_2	$\sigma_{\mathrm{a},2}$	ZP	σ_{ZP}
r	$V-R$	0.094	0.038	−0.239	0.044	19.969	0.008
	$R-I$	0.113	0.034	−0.269	0.041	19.976	0.007
g	$B-V$	−0.110	0.018	−0.030	0.012	20.443	0.006
	$V-R$	−0.280	0.034	−0.034	0.041	20.462	0.007
b	$U-B$	0.158	0.009	−0.011	0.007	21.242	0.007
	$B-V$	0.185	0.019	0.019	0.015	21.147	0.006

Table 12: Final results for the application of χ^2-minimization to the quadratic case in Equation 16. Final results are for the color transformation coefficients a_1 and a_2 and the zero point ZP for filters r, g, and b and related color indices C. $\sigma_{\mathrm{a},1}$, $\sigma_{\mathrm{a},2}$, and σ_{ZP} are the corresponding uncertainties.

filter	C	a_1	$\sigma_{\mathrm{a},1}$	a_2	$\sigma_{\mathrm{a},2}$	ZP	σ_{ZP}
r	$V-R$	0.095	0.038	−0.235	0.044	19.970	0.007
	$R-I$	0.057	0.034	−0.195	0.041	19.972	0.007
g	$B-V$	−0.136	0.018	−0.021	0.017	20.455	0.006
	$V-R$	−0.246	0.034	−0.076	0.041	20.460	0.007
b	$U-B$	0.162	0.009	−0.014	0.007	21.243	0.007
	$B-V$	0.190	0.019	0.018	0.015	21.146	0.006

Table 13: Results from a stability check of the solution from the quadratic χ^2-minimization. The input parameter $m_{\mathrm{instr},0}$ was replaced by random values from a Gaussian distribution, which was centered on the real value with a standard deviation corresponding to the uncertainty σ_{m}. From 10000 minimization runs for each filter-color combination the mean and the standard deviation were computed and are listed here.

I also produced plots for the correlation between the datapoints for every filter-color combination and both the linear and quadratic fit. They are shown in Figures 26-31. The following paragraphs discuss and compare the results.

General remarks about the final results from the linear fit (Table 11): The values for the transformation coefficient a and the zero point ZP cannot directly be compared to measurements from other observers, because they are characteristic for the transformation between the Baader and the Landolt system[24]. Results can mostly be considered plausible. Transformation coefficients are small but not extremely small for filters g and b. I consider this realistic because the bandwidth and central wavelength of the filters is similar to the V and B filters from the standard system (compare Figures 4 and 5). For filter r my expectation was that the absolute value of the transformation coefficient would be bigger, because especially the R filter used by Landolt has a significantly broader transmission curve than the Baader r filter (compare Figures 4 and 5). Possible explanations will be discussed below. Uncertainties for all filters are reasonable or even a bit low, considering the expected precision of a fit applied to only five datapoints. The small uncertainties of the zero points are due to the linear influence of the zero point on the result. Linear terms are less sensitive to changes than multiplicative ones like the transformation coefficients. In the plots (Figures 26-31) it can be seen that the fit solutions for filter g and b are based on actual correlations between the magnitude difference $m_{\mathrm{lit,i}} - m_{\mathrm{instr,i}}$ and the related color indices. That is why the datapoints show a linear relation and produce a stable linear fit. This is not the case for filter r. The correlation plot for the r filter does not show a predominantly linear behavior because the datapoints form a shapeless cluster. Considering that there are many possbilities to fit a linear curve through a cluster of datapoints, it is probable that the obtained fit is not correct or close to the real solution. In the following I will concentrate on statements and conclusions about results for filter g and b. Filter r data cannot be considered reliable for any general judgement and will be discussed seperately.

General remarks about the final results from the quadratic fit (Table 12) and cross-check (Table 13): The results are consistent for filters g and b, since the second order transformation coefficient is smaller by roughly an order of magnitude than the first order coefficient. Again, values and uncertainties for filter g and b seem realistic, except for the uncertainties of the second order transformation coefficient for filter g and b, which are quite big. All results are reproduced inside of the error intervals by the cross-check. The conclusion is that the uncertainties are actually as big. My theory is that I am trying to fit an effect that is too small for the achieved precision. The spread of the datapoints in Figures 28, 29, 30, and 31 for filter g and b and more importantly the sample size suggest that the measurement did not reach enough precision for a small effect like the quadratic term to come through without big uncertainties. It is like trying to extract a signal from a CCD image that is smaller than the background fluctuations (see section 3.4). Filter r values are not at all consistent among themselves

[24] I also looked for data from other photometric calibrations using the Baader filter system, but could not find any. A likely reason is that the Baader filters are mostly used for astrophotography and not conceived for photometric measurements. The equipment that was used for this bachelor thesis was originally thought to be used for the guiding of the 11-inch telescope, not for actual measurements. Therefore it is not the typical equipment for photometry purposes.

since the second order coefficient absolute value is significantly bigger than the first order coefficient.

Comparison of linear and quadratic fit for filter r: The results for the first order transformation coefficient show a dramatic difference between the linear and quadratic solution. Figures 26 and 27 both demonstrate how far apart the solutions are and why the second order transformation coefficient has so much more weight in the quadratic solution. The clustered datapoints do not really resemble any typical curve by eyesight, but from the point of view of the least squares minimization, a parabola seems to be closer to the datapoints than a linear curve. It is clear that the very low number of datapoints is one of the major problems here. It cannot be the only problem because then the results for filter g and b would be as bad. Probably the bad results for filter r are due to several effects combined: The small sample of stars, systematic uncertainties in the analysis, especially from the manual application of the growing curve correction, and the additional complication because of the differences between the Baader r filter and Landolt R filter. Another possibly related effect is the strong gradient in the transmission of the r filter. This can be seen on the two flat frames in Figure 12 from section 3.4. None of the other filters showed such a strong gradient. Since the application of master flat frames was found to not remove the vignetting completely (see section 4.2.3) it could be that the remaining gradient and vignetting was stronger for the r filter. This could have caused significant differences in the background estimation and propagated through the calculation, resulting in the scattered datapoints.

Comparison of linear and quadratic fit for filters g and b: The combined results from the linear and quadratic fit match the expectation. First order transformation coefficients for the quadratic fit are a bit smaller than the ones from the linear fit in most cases, because a part of the contribution comes from the quadratic term. The fit curves in Figures 28, 29, 30, and 31 mostly look very similar for the linear and quadratic case, with the exception of the fit for filter g and color $B-V$. The second transformation coefficient is a bit bigger for that combination, possibly because of the most distant datapoint with the largest errorbar (see next paragraph).

I noticed one of the datapoints in each of the six plots is always farthest away from the fit curves and has the biggest errorbar. The datapoints all correspond to the same star SA 96 36 with a $B-V$ color index of 0.247 (see Table 10). The datapoints always lie below the fit curves at a smaller magnitude difference, indicating that the instrumental magnitude m_{instr} was underestimated. I checked different steps of the SA 96 36 analysis again and came to the conclusion that another star, which I thought far enough away for a reliable background estimation, was actually too close to SA 96 36. The background I selected seems to have included some starlight from SA 96 36 and possibly the neighbor star, leading to an overestimation of the background and an underestimation of the total count. It could be interesting later to repeat the analysis of SA 96 36 using the masking option of the growing curve program. Apparently this worked well for SA 99 438, since the datapoints do not stand out in an any way[25].

Conclusions from the discussion of the final results are the following: Filter r data shows significant discrepancies. The necessary conclusion has to be that the corresponding transformation relation cannot be used for any further measurements, because it is not reliable. The results for filter g and b leave room for improvement of the precision, but are nevertheless a good first result. With the achieved precision the results from the linear fit should be chosen over the ones from the quadratic fit for further use in measurements of the transmission. The most important understanding of the above evaluation is the need for more stars in the calibration measurement. More target stars can provide more stability in the fit solution, will reduce uncertainties, and make a higher order fitting possible [37]. The growing curve method alone is not sufficient in many cases because fields are too crowded to allow a correct background estimation. New approaches or additional steps like the pixel masking have to be applied to make this analysis step more reliable. In the conclusion, I will summarize the work of this Bachelor thesis and give an outlook on further steps anticipated with the MAM.

[25]But this is only one single case. For a real evaluation of the masking option more tests are needed.

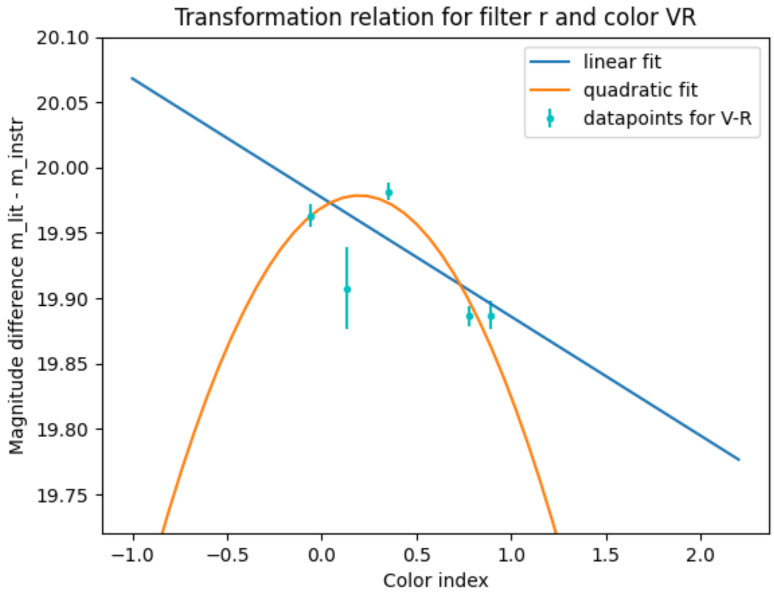

Figure 26: The plot shows the transformation relation for filter r and the strength of correlation between the magnitude difference $m_{\mathrm{lit,r,i}} - m_{\mathrm{instr,r,i}}$ and the related color index $(V - R)$. The magnitudes are named according to Equation 14.

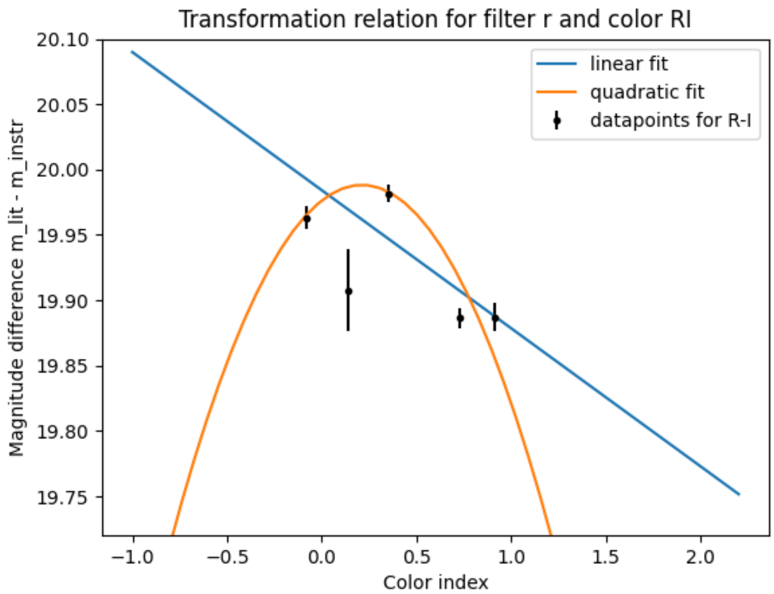

Figure 27: Transformation relation like in Figure 26 for filter r with magnitude difference $m_{\mathrm{lit,r,i}} - m_{\mathrm{instr,r,i}}$ and related color index $(R - I)$.

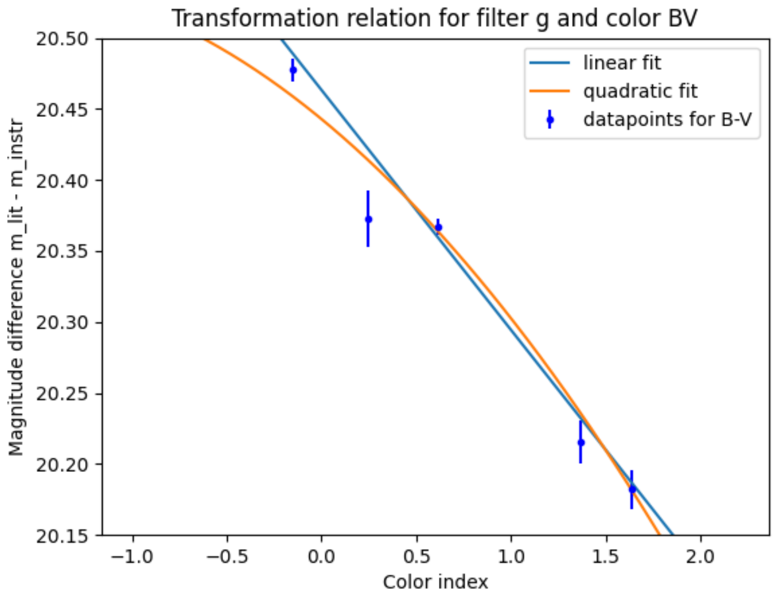

Figure 28: Transformation relation like in Figure 26 for filter g with magnitude difference $m_{\mathrm{lit,g,i}} - m_{\mathrm{instr,g,i}}$ and related color index $(B - V)$.

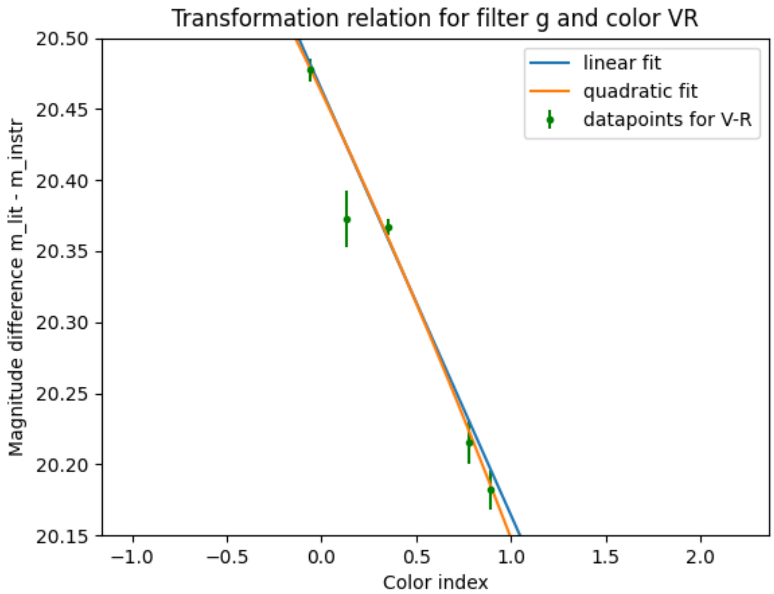

Figure 29: Transformation relation like in Figure 26 for filter g with magnitude difference $m_{\mathrm{lit,g,i}} - m_{\mathrm{instr,g,i}}$ and related color index $(V - R)$.

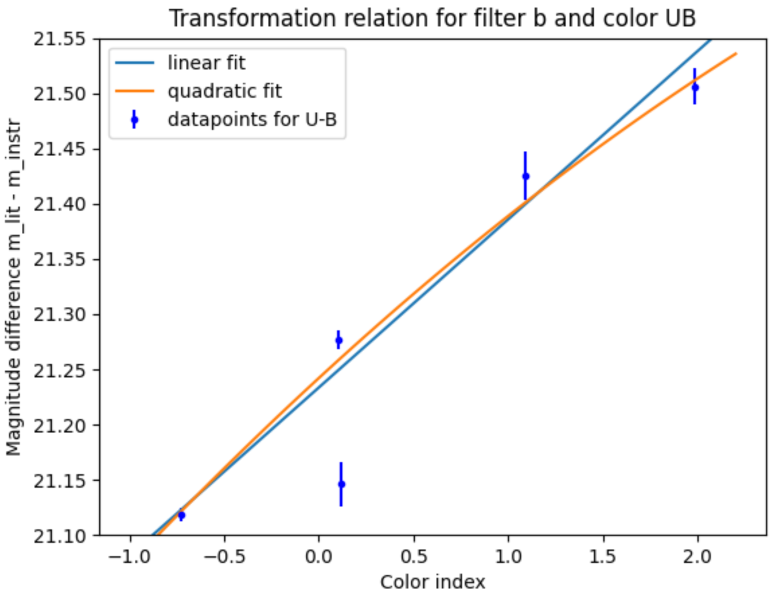

Figure 30: Transformation relation like in Figure 26 for filter b with magnitude difference $m_{\mathrm{lit,b,i}} - m_{\mathrm{instr,b,i}}$ and related color index $(U - B)$.

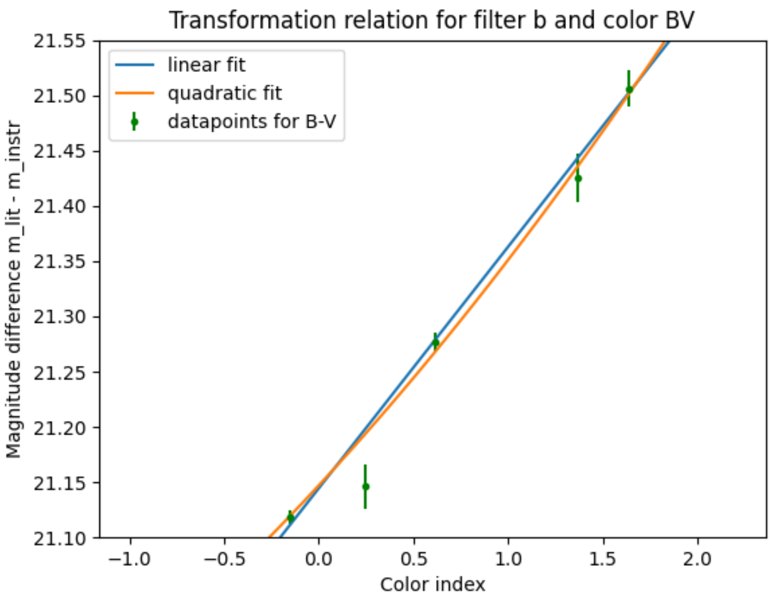

Figure 31: Transformation relation like in Figure 26 for filter b with magnitude difference $m_{\mathrm{lit,b,i}} - m_{\mathrm{instr,b,i}}$ and related color index $(B - V)$.

5 Conclusion and Outlook

In this Bachelor thesis I have calibrated the photometric system of the MAM telescope with respect to the Landolt standard photometric system. Extinction coefficients in different bands of the visible spectrum were determined and the transformation relations between the photometric systems derived. With the result of this Bachelor thesis it is now possible to perform a first transmission measurement using the new transformation relations and then comparing transmission values to measurements from other instruments like the LIDAR. This will be an additional trial for the end results in filter g and b. I have provided information on the question: What is the best way to realize photometric measurements with the MAM telescope taking into account special operation conditions, like high zenith angles and imperfect weather conditions? Two approaches were considered: Using an existing catalog of standard stars to calibrate the MAM's photometric system, like I did in this thesis, or creating a catalog with MAM. I consider the results from the calibration promising because of the following reason: For filter g and b, the calculation of the transformation relations gave consistent and stable results, even though they were based on a very small sample of stars. In order to avoid reproducing inconsistent results in filter r and to increase the precision of the measurements, further improvements to my work could be: Most importantly a photometric calibration needs to use a bigger sample of stars to achieve reliable transformation relations. The interval for the background estimation has to be selected more carefully for the case of a nearby star close to the target star or other methods have to be applied for crowded fields, for example pixel masking. Data reduction techniques can be improved to avoid hot pixels and a non-uniform background. For an extrapolation of airmass zero it is more reliable to exclude datapoints at large zenith angles and only take measurements between airmass 1 and $3-4$.

The ideas for improvements result from questions that arose during this work and still have to be answered in the future: How can aperture photometry be done in crowded star fields? Can the growing curve correction be automated? Why were there hot pixels left in the reduced light frames, although the camera was cooled to the same temperature for the dark frames? What caused the inconsistent results in the red filter? Why is the focus of the camera changing gradually? What causes the smeared star images at a zenith angle of $30\,^\circ$, pointing towards the celestial equator? Can better results be achieved with other filters, suited for photometry?

Answering these questions will advance the MAM project and provide further information on the applicability of the photometric concepts. The concept based on an existing catalog is more complex and needs a lot of effort and observational time to realize as this work has shown, but it might be a more general way to achieve the long-term goal of MAM. On the other hand, the concept of building a catalog with MAM successively by starting only with a few MAGIC VLZA observations is a lot easier and needs less effort for quicker first results. It is also less susceptible to systematic effects that can arise from the photometric transformation between systems. In spite of the different realizations of the task of MAM, the two concepts have a base in common. Both require a reliable measurement of star fluxes. Big parts of the considerations in this work and the implemented code will therefore be useful in both cases. No matter which concept will be realized in near future, the work on the optical MAM telescope will stay interesting because of the special conditions in which it will be operated: Supporting the search for VHE gamma rays by observing PeVatron candidate sources at VLZA.

A Appendix

A.1 Airmass plots

A.1.1 SA 92-312

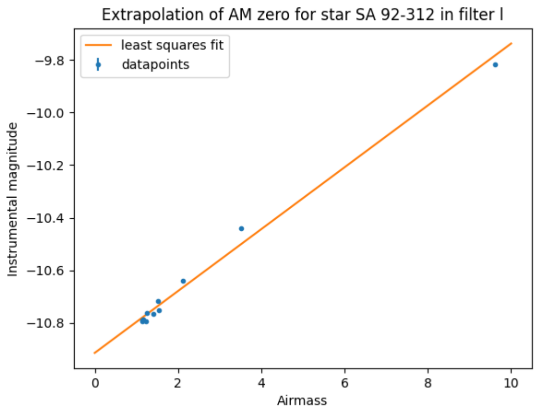

(a) With all datapoints

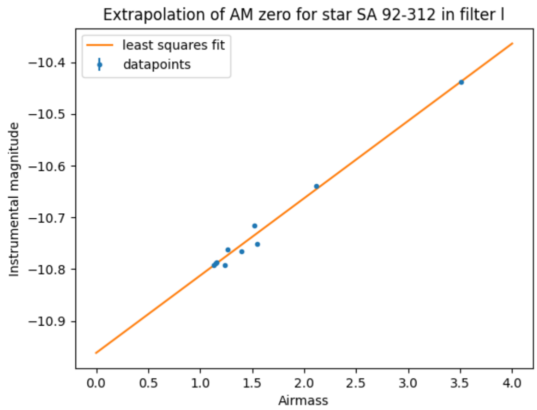

(b) Without datapoint 11

Figure 32: Extrapolation of AM zero for star SA 92-312 (filter l)

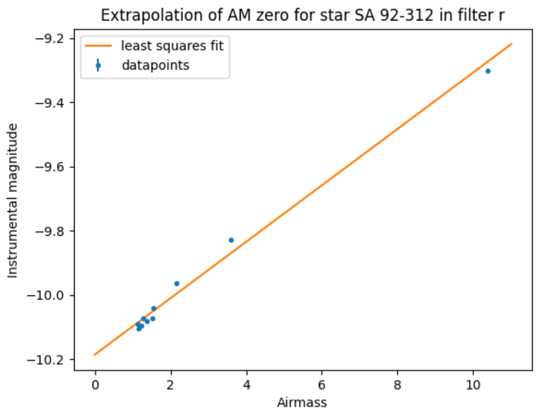

Figure 33: Extrapolation of AM zero for star SA 92-312 (filter r)

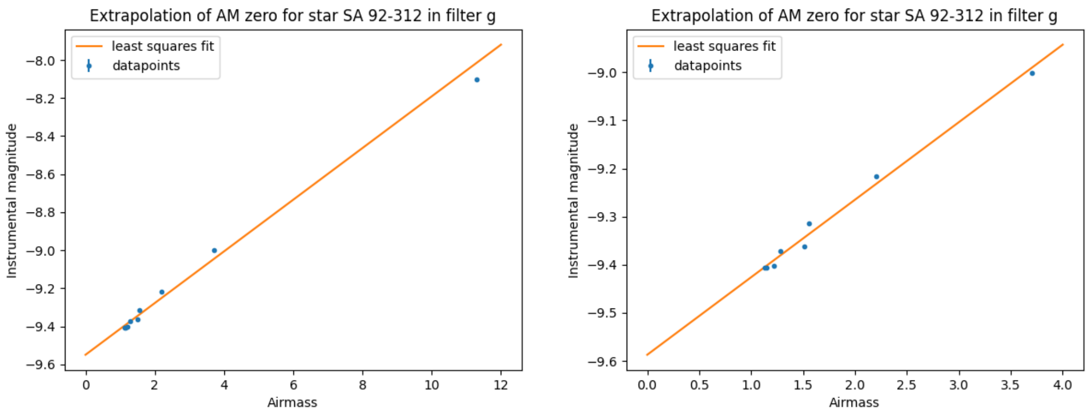

(a) With all datapoints

(b) Without datapoint 10

Figure 34: Extrapolation of AM zero for star SA 92-312 (filter g)

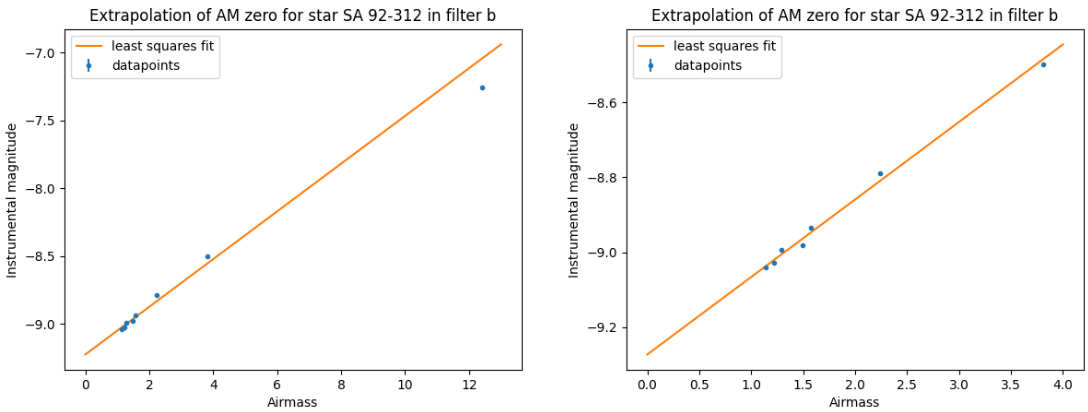

(a) With all datapoints

(b) Without datapoint 9

Figure 35: Extrapolation of AM zero for star SA 92-312 (filter b)

A.1.2 SA 96 36

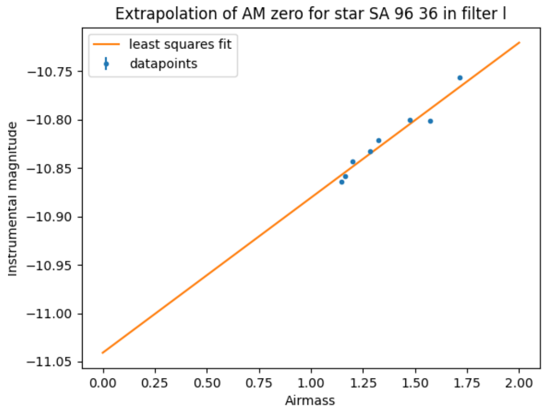

Figure 36: Extrapolation of AM zero for star SA 96 36 (filter l)

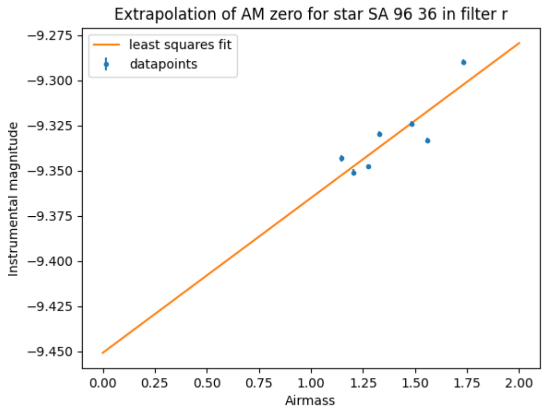

Figure 37: Extrapolation of AM zero for star SA 96 36 (filter r)

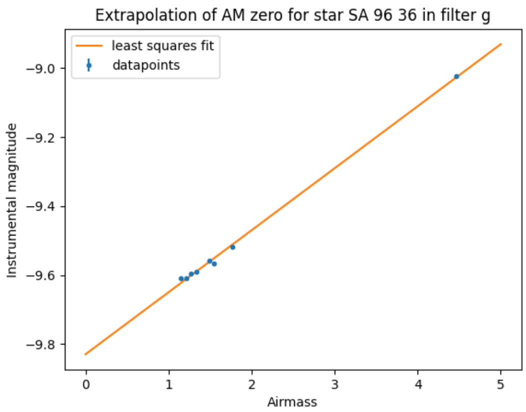

(a) With all datapoints

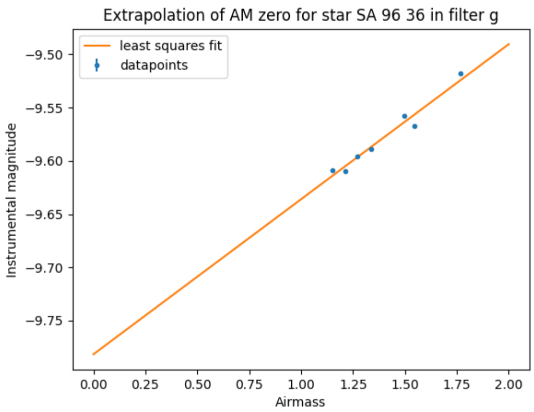

(b) Without datapoint 10

Figure 38: Extrapolation of AM zero for star SA 96 36 (filter g)

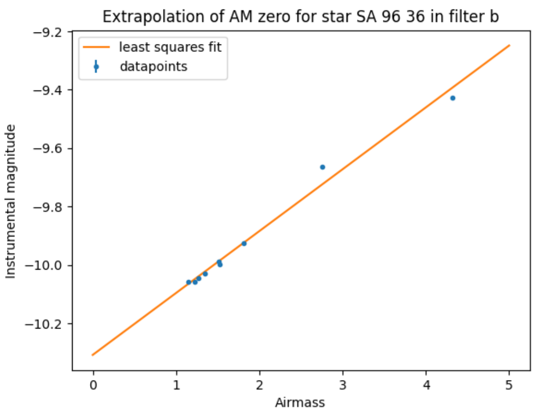

Figure 39: Extrapolation of AM zero for star SA 96 36 (filter b)

A.1.3 SA 97 284

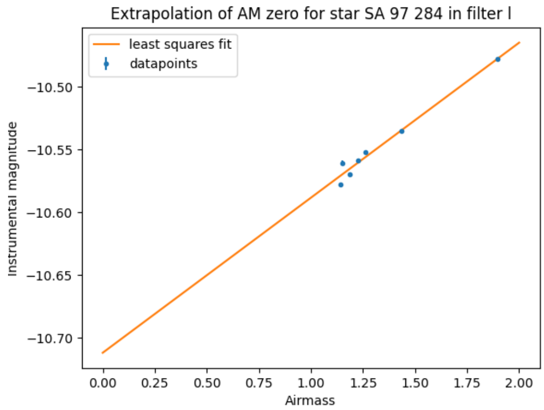

Figure 40: Extrapolation of AM zero for star SA 97 284 (filter l)

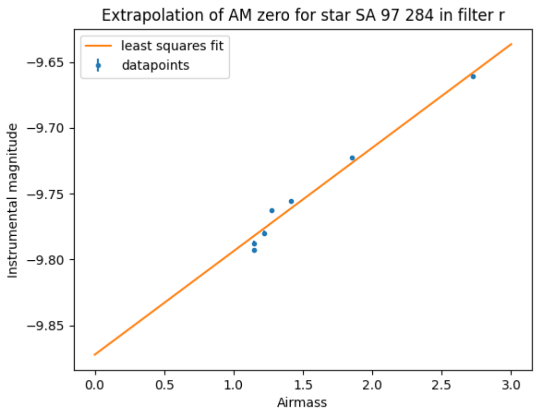

Figure 41: Extrapolation of AM zero for star SA 97 284 (filter r)

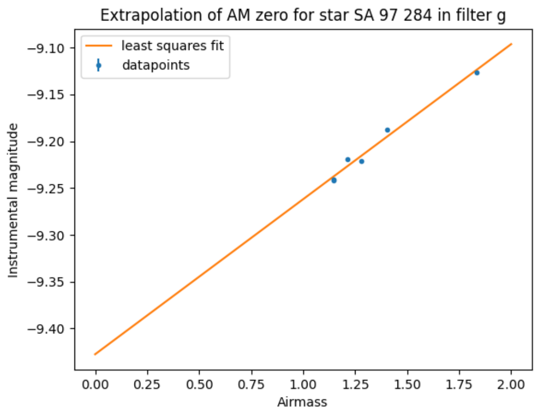

Figure 42: Extrapolation of AM zero for star SA 97 284 (filter g)

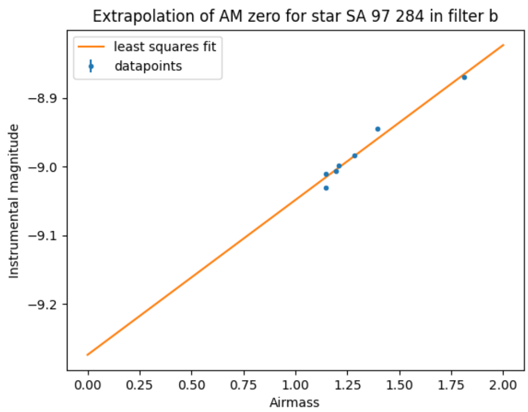

Figure 43: Extrapolation of AM zero for star SA 97 284 (filter b)

A.1.4 SA 99 438

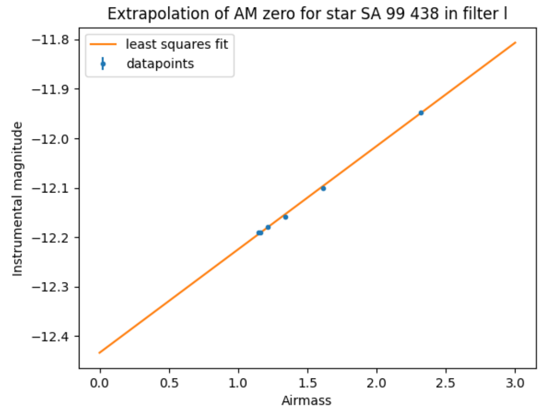

Figure 44: Extrapolation of AM zero for star SA 99 438 (filter l)

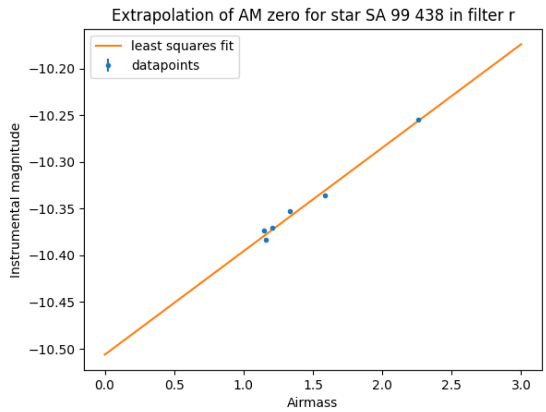

Figure 45: Extrapolation of AM zero for star SA 99 438 (filter r)

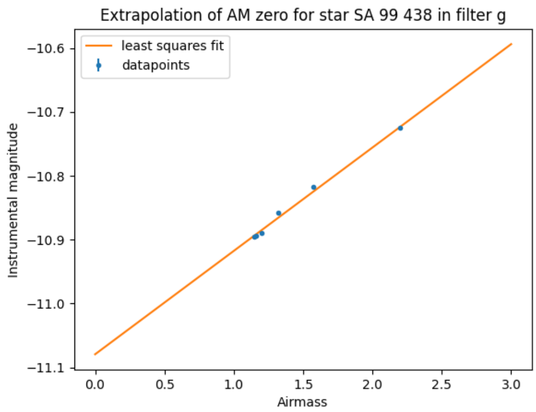

Figure 46: Extrapolation of AM zero for star SA 99 438 (filter g)

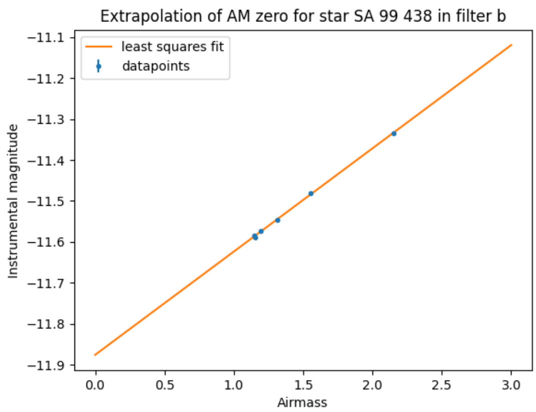

Figure 47: Extrapolation of AM zero for star SA 99 438 (filter b)

A.1.5 SA 115 271

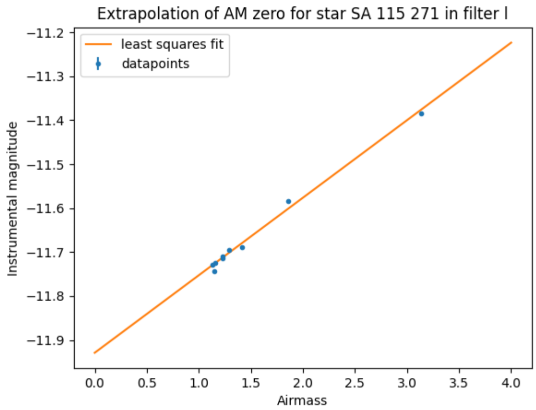

Figure 48: Extrapolation of AM zero for star SA 115 271 (filter l)

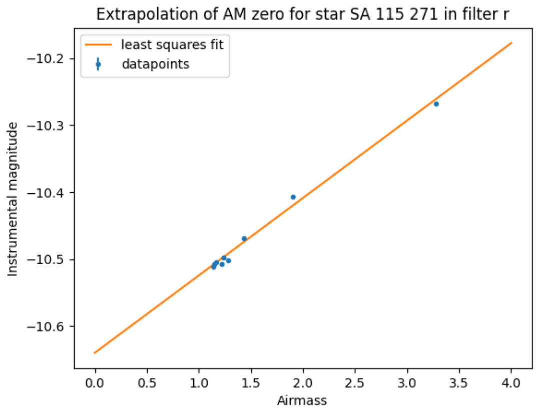

Figure 49: Extrapolation of AM zero for star SA 115 271 (filter r)

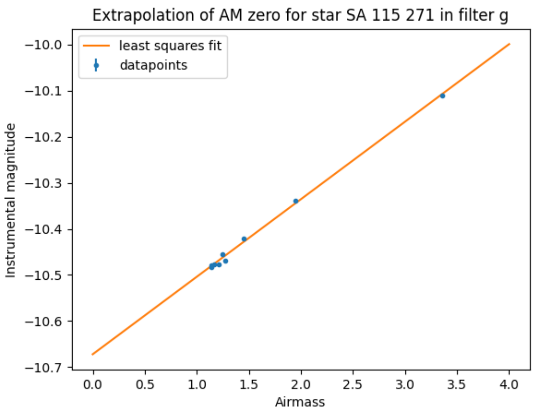

Figure 50: Extrapolation of AM zero for star SA 115 271 (filter g)

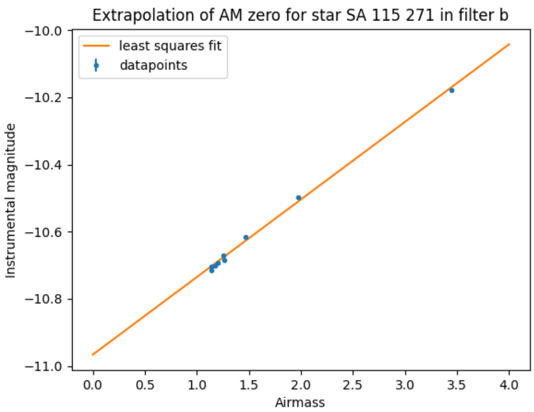

Figure 51: Extrapolation of AM zero for star SA 115 271 (filter b)

A.2 Derivations for χ^2 minimization

According to section 3.3 and the derivation in [36], the χ^2-function for the case of the second order magnitude transformation is:

$$\chi^2 = \sum_{i=1}^{N} \frac{[y_\mathrm{i} - (ZP + x_\mathrm{i} + a_1 C_\mathrm{i} + a_2 C_\mathrm{i}^2)]^2}{\sigma_\mathrm{i}^2}. \tag{27}$$

In the equation above i is the index, iterating over the five stars that were observed, so $N = 5$. y_i is the catalog magnitude of star i (at AM zero), ZP is the zero point of the observing system, x_i is the measured instrumental magnitude (at AM zero), a_1 is the color transformation coefficient with respect to the linear color index term C_i, a_2 is the color transformation coefficient with respect to the quadratic color index term C_i^2 and σ_i is the uncertainty of the measured quantity x_i. The zero point and the two transformation coefficients are the quantities that have to be determined by the fit. Taking the derivative of χ^2 after each of these and setting it equal to zero yields:

$$\frac{\partial \chi^2}{\partial a_1} = -2 \sum_{i}^{N} \frac{[y_\mathrm{i} - (ZP + x_\mathrm{i} + a_1 C_\mathrm{i} + a_2 C_\mathrm{i}^2)] C_\mathrm{i}}{\sigma_\mathrm{i}^2} \overset{!}{=} 0, \tag{28}$$

$$\frac{\partial \chi^2}{\partial a_2} = -2 \sum_{i}^{N} \frac{[y_\mathrm{i} - (ZP + x_\mathrm{i} + a_1 C_\mathrm{i} + a_2 C_\mathrm{i}^2)] C_\mathrm{i}^2}{\sigma_\mathrm{i}^2} \overset{!}{=} 0, \tag{29}$$

$$\frac{\partial \chi^2}{\partial ZP} = -2 \sum_{i}^{N} \frac{[y_\mathrm{i} - (ZP + x_\mathrm{i} + a_1 C_\mathrm{i} + a_2 C_\mathrm{i}^2)]}{\sigma_\mathrm{i}^2} \overset{!}{=} 0. \tag{30}$$

The three equations form a linear equation system which can be rearranged and written as a matrix equation

$$Ax = b \tag{31}$$

where

$$\mathrm{A} := \begin{pmatrix} A_{11} & A_{12} & A_{13} \\ A_{21} & A_{22} & A_{23} \\ A_{31} & A_{32} & A_{33} \end{pmatrix} := \begin{pmatrix} \sum_i^N \frac{C_\mathrm{i}^2}{\sigma_\mathrm{i}^2} & \sum_i^N \frac{C_\mathrm{i}^3}{\sigma_\mathrm{i}^2} & \sum_i^N \frac{C_\mathrm{i}}{\sigma_\mathrm{i}^2} \\ \sum_i^N \frac{C_\mathrm{i}^3}{\sigma_\mathrm{i}^2} & \sum_i^N \frac{C_\mathrm{i}^4}{\sigma_\mathrm{i}^2} & \sum_i^N \frac{C_\mathrm{i}^2}{\sigma_\mathrm{i}^2} \\ \sum_i^N \frac{C_\mathrm{i}}{\sigma_\mathrm{i}^2} & \sum_i^N \frac{C_\mathrm{i}^2}{\sigma_\mathrm{i}^2} & \sum_i^N \frac{1}{\sigma_\mathrm{i}^2} \end{pmatrix},$$

$$\text{b} := \begin{pmatrix} b_1 \\ b_2 \\ b_3 \end{pmatrix} := \begin{pmatrix} \sum_i^N \frac{(y_\mathrm{i}-x_\mathrm{i})C_\mathrm{i}}{\sigma_\mathrm{i}^2} \\ \sum_i^N \frac{(y_\mathrm{i}-x_\mathrm{i})C_\mathrm{i}^2}{\sigma_\mathrm{i}^2} \\ \sum_i^N \frac{(y_\mathrm{i}-x_\mathrm{i})}{\sigma_\mathrm{i}^2} \end{pmatrix}, \text{ and x} := \begin{pmatrix} a_1 \\ a_2 \\ ZP \end{pmatrix}.$$

I solved the system in two ways, first using the linalg.lstsq method from the python module numpy, then solving it analytically. The uncertainties could only be determined analytically and since this meant solving the whole system first, I repeated the calculation of end results with the analytical solution. Both gave the same results. The analytical solution is as follows:

$$a_1 = B^1_{\mathrm{a},1} b_1 + B^2_{\mathrm{a},1} b_2 + B^3_{\mathrm{a},1} b_3, \tag{32}$$

$$a_2 = B^1_{\mathrm{a},2} b_1 + B^2_{\mathrm{a},2} b_2 + B^3_{\mathrm{a},2} b_3, \tag{33}$$

$$ZP = B^1_{ZP} b_1 + B^2_{ZP} b_2 + B^3_{ZP} b_3, \tag{34}$$

where I define

$$L := (A_{12} - \frac{A_{11}A_{32}}{A_{31}}) - (A_{13} - \frac{A_{11}A_{33}}{A_{31}})(A_{22} - \frac{A_{21}A_{32}}{A_{31}})(A_{23} - \frac{A_{21}A_{33}}{A_{31}})^{-1}, \tag{35}$$

$$B^1_{\mathrm{a},2} := \frac{1}{L}, \tag{36}$$

$$B^2_{\mathrm{a},2} := -\frac{1}{L}(A_{13} - \frac{A_{11}A_{33}}{A_{31}})(A_{23} - \frac{A_{21}A_{33}}{A_{31}})^{-1}, \tag{37}$$

$$B^3_{\mathrm{a},2} := \frac{1}{L}[-\frac{A_{11}}{A_{31}} + (A_{13} - \frac{A_{11}A_{33}}{A_{31}})(A_{23} - \frac{A_{21}A_{33}}{A_{31}})^{-1}], \tag{38}$$

$$B^1_{ZP} := -B^1_{\mathrm{a},2}(A_{22} - \frac{A_{21}A_{32}}{A_{31}})(A_{23} - \frac{A_{21}A_{33}}{A_{31}})^{-1}, \tag{39}$$

$$B^2_{ZP} := -[1 + B^2_{\mathrm{a},2}(A_{22} - \frac{A_{21}A_{32}}{A_{31}})](A_{23} - \frac{A_{21}A_{33}}{A_{31}})^{-1}, \tag{40}$$

$$B^3_{ZP} := -[\frac{A_{21}}{A_{A31}} + B^3_{\mathrm{a},2}(A_{22} - \frac{A_{21}A_{32}}{A_{31}})](A_{23} - \frac{A_{21}A_{33}}{A_{31}})^{-1}, \tag{41}$$

$$B^1_{\mathrm{a},1} := \frac{-(A_{32}B^1_{\mathrm{a},2} + A_{33}B^1_{ZP})}{A_{31}}, \tag{42}$$

$$B^2_{\mathrm{a},1} := \frac{-(A_{32}B^2_{\mathrm{a},2} + A_{33}B^2_{ZP})}{A_{31}}, \tag{43}$$

$$B^3_{\mathrm{a},1} := \frac{1 - (A_{32}B^3_{\mathrm{a},2} + A_{33}B^3_{ZP})}{A_{31}}. \tag{44}$$

A_{ij} are the matrix elements of matrix A, defined before. The calculation of the uncertainties was classic Gaussian error propagation:

$$\sigma_{\mathrm{a},1} = \sum_{i}^{N} \sigma_{\mathrm{i}}^2 (\frac{\partial a_1}{\partial x_{\mathrm{i}}})^2 \tag{45}$$

with

$$\frac{\partial a_1}{\partial x_{\mathrm{i}}} = -B_{\mathrm{a},1}^1 \frac{C_{\mathrm{i}}}{\sigma_{\mathrm{i}}^2} - B_{\mathrm{a},1}^2 \frac{C_{\mathrm{i}}^2}{\sigma_{\mathrm{i}}^2} - B_{\mathrm{a},1}^3 \frac{1}{\sigma_{\mathrm{i}}^2}, \tag{46}$$

$$\sigma_{\mathrm{a},2} = \sum_{i}^{N} \sigma_{\mathrm{i}}^2 (\frac{\partial a_2}{\partial x_{\mathrm{i}}})^2 \tag{47}$$

with

$$\frac{\partial a_2}{\partial x_{\mathrm{i}}} = -B_{\mathrm{a},2}^1 \frac{C_{\mathrm{i}}}{\sigma_{\mathrm{i}}^2} - B_{\mathrm{a},2}^2 \frac{C_{\mathrm{i}}^2}{\sigma_{\mathrm{i}}^2} - B_{\mathrm{a},2}^3 \frac{1}{\sigma_{\mathrm{i}}^2}, \tag{48}$$

$$\sigma_{ZP} = \sum_{i}^{N} \sigma_{\mathrm{i}}^2 (\frac{\partial ZP}{\partial x_{\mathrm{i}}})^2 \tag{49}$$

with

$$\frac{\partial ZP}{\partial x_{\mathrm{i}}} = -B_{ZP}^1 \frac{C_{\mathrm{i}}}{\sigma_{\mathrm{i}}^2} - B_{ZP}^2 \frac{C_{\mathrm{i}}^2}{\sigma_{\mathrm{i}}^2} - B_{ZP}^3 \frac{1}{\sigma_{\mathrm{i}}^2}. \tag{50}$$

B Appendix

Camera technical details

Sensor	4/3″ CMOS
Diagonal	21.9mm
Resolution	16Mega Pixels 4656×3520
Pixel Size	3.8μm
Image area	17.6mm*13.3mm
Max FPS at full resolution	23FPS(10bitADC) 15FPS(12bitADC)
Shutter	Rolling shutter
Exposure Range	32μs-2000s
Read Noise	1.2e @30db gain
QE peak	~60%
Full well	20ke
ADC	12 bit or 10 bit
DDR3 buffer	256MB
Interface	USB3.0/USB2.0
Adapters	2″ / 1.25″ / M42X0.75
Protect window	AR window
Dimensions	Uncooled 62mm/Cooled 78mm
Weight	Uncooled 140g/Cooled 410g
Back Focus Distance	6.5mm
Cooling:	Regulated Two Stage TEC
Delta T	40°C -45°C below ambient
Cooling Power consumption	12V at 2A Max
Supported OS	Windows, Linux & Mac OSX
Working Temperature	-5°C—45°C
Storage Temperature	-20°C—60°
Working Relative Humidity	20%—80%
Storage Relative Humidity	20%—95%

Figure 52: Technical information on the ASI1600mm cool camera from ZWO. Datasheet from [44].

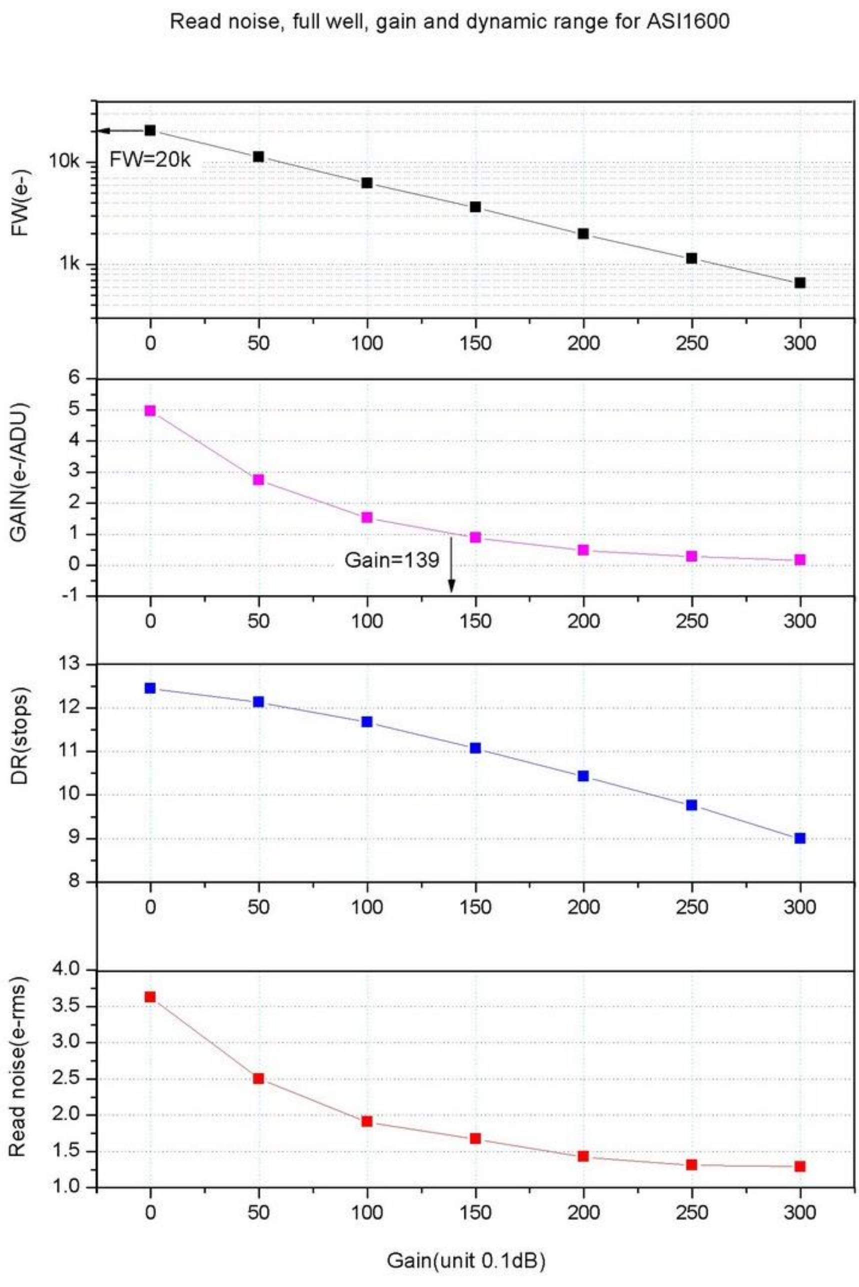

Figure 53: Read noise, Dynamic Range (DR), Gain, and Full Well capacity (FW) against Gain in units of dB. Graphs from [44].

Bibliography

[1] Adam, J., Bruss, J., Brügge, K., Nöthe, M., and Rhode, W. Cloud Detection and Prediction with All Sky Cameras. *EPJ Web of Conferences*, vol. 144, 2017. doi:10.1051/epjconf/201714401004.

[2] Die Baader L-RGB-C CCD-Filter | Baader Planetarium Blog Beiträge (accessed on 04-12-2020).
URL `https://www.baader-planetarium.com/de/blog/die-baader-l-rgb-c-ccd-filter/`

[3] Bessel, M. S. UBVRI passbands. *Publications of the Astronomical Society of the Pacific*, vol. 102:1181–1199, 1990. doi:10.1086/132749.

[4] Bessel, M. S. Standard Photometric Systems. *Annual Review of Astronomy & Astrophysics*, vol. 43(1):293–336, 2005. doi:10.1146/annurev.astro.41.082801.100251.

[5] Bindel, A. Atmospheric Transmission on the Wendelstein Observatory. Master's thesis, Ludwig–Maximilians University (LMU) Munich, 2011.

[6] Burki, G., et al. The atmospheric extinction at the E.S.O. La Silla Observatory. *Astronomy and Astrophysics Supplement Series*, vol. 112:383–394, 1995.

[7] DaCosta, G. S. Basic Photometry Techniques. *ASP Conference Series*, vol. 23, 1992.

[8] Ebr, J., et al. Characterization of atmospheric properties at the future sites of the Cherenkov Telescope Array. In Proceedings of Science. 2019. International Cosmic Ray Conference (ICRC).

[9] Fellers, T. J. and Davidson, M. W. Hamamatsu Learning Center: CCD Noise Sources and Signal-to-Noise Ratio (accessed on 02-12-2020).
URL `https://hamamatsu.magnet.fsu.edu/articles/ccdsnr.html`

[10] Fruck, C. The Galactic Center resolved with MAGIC and a new technique for Atmospheric Calibration. Ph.D. thesis, Technical University Munich (TUM), 2015.

[11] Gaisser, T. K., Engel, R., and Resconi, E. Cosmic Rays and Particle Physics (Cambridge University Press), 2016.

[12] Helmer, L. The Carlsberg Automatic Meridian Circle: La Palma. *Astrophysical Letters & Communications*, vol. 28:101–112, 1991.

[13] Hoff, D. Programming and Installation of a New 11-inch Telescope Subsystem for MAGIC. Master's thesis, Technical University Munich (TUM), 2020.

[14] Hoff, D. and Pihet, M. Git repository of the MAM-Telescope control software (No public access).
URL `https://git.fs.lmu.de/mpihet/mam`

[15] Howell, S. B. Two-Dimensional Aperture Photometry: Signal-to-Noise Ratio of Point-Source Observations and Optimal Data-Extraction Techniques. *Publications of the Astronomical Society of the Pacific*, vol. 101:616–622, 1989. doi:10.1086/132477.

[16] Howell, S. B. Handbook of CCD Astronomy (Cambridge University Press), 2 edn., 2006.

[17] Ilovaisky, S. Optical Photometry. 5th NEON Observing School, 2006. Haute-Provence Observatory (OHP).

[18] Johnson, H. L. Astronomical Measurements in the Infrared. *Annual Review of Astronomy & Astrophysics*, vol. 4:193–206, 1966. doi:10.1146/annurev.aa.04.090166.001205.

[19] Johnson, H. L. and Morgan, W. W. Fundamental Stellar Photometry for Standards of Spectral Type on the Revised System of the Yerres Spectral Altas*. *The Astrophysical Journal*, vol. 117(3):313–352, 1953. doi:10.1086/145697.

[20] Jordi, K., Grebel, E. K., and Ammon, K. Empirical color transformations between SDSS photometry and other photometric systems. *Astronomy & Astrophysics*, vol. 460(1):339–347, 2006. doi:10.1051/0004-6361:20066082.

[21] Kasten, F. and Young, A. T. Revised optical air mass tables and approximation formula. *Applied Optics*, vol. 28(22):4735–4738, 1989. doi:10.1364/AO.28.004735.

[22] Laken, B. A., P, H., Parviainen, H., Pallé, E., and Shahbaz, T. Saharan mineral dust outbreaks observed over the North Atlantic island of La Palma in summertime between 1984 and 2012. *Quarterly Journal of the Royal Meteorological Society*, vol. 140(680):1058–1068, 2014.

[23] Landolt, A. U. UBV photoelectric sequences in the celestial equatorial Selected Areas 92-115. *The Astronomical Journal*, vol. 78(9):959–981, 1973. doi:10.1086/111503.

[24] Landolt, A. U. UBVRI Photometric standard stars around the celestial equator. *The Astronomical Journal*, vol. 88(3):439–460, 1983. doi:10.1086/113329.

[25] Landolt, A. U. UBVRI Photometric Standard Stars in the Magnitude Range $11.5 < V < 16.0$ Around the Celestial Equator. *The Astronomical Journal*, vol. 104(1):340–491, 1992. doi:10.1086/116242.

[26] Landolt, A. U. UBVRI Photometric Standard Stars Around the Sky at -50 Degrees Declination. *The Astronomical Journal*, vol. 133(6):2502–2523, 2007. doi:10.1086/518000.

[27] Landolt, A. U. UBVRI Photometric Standard Stars Around the Celestial Equator: Updates and Additions. *The Astronomical Journal*, vol. 137(5):4186–4269, 2009. doi:10.1088/0004-6256/137/5/4186.

[28] Lim, B., Sung, H., Bessel, M. S., Karimov, R., and Ibrahimov, M. CCD Photometry of Standard Stars at Maidanak Astronomical Observatory in Uzbekstan: Transformations and Comparisons. *Journal of the Korean Astronomical Society*, vol. 42(6):161–174, 2009. doi:10.5303/JKAS.2009.42.6.161.

[29] MAGIC Collaboration, Daily Data Check (No public access, accessed on 25-11-2020).
URL `http://www.magic.iac.es/operations/datacheck`

[30] Miles, R. A light history of photometry: from Hipparchus to the Hubble Space Telescope. *Journal of the British Astronomical Association*, vol. 117(4):172–186, 2007.

[31] Mirzoyan, R., et al. Extending the observation limits of Imaging Air Cherenkov Telescopes toward horizon. *Nuclear Instruments and Methods in Physics Research Section A: Accelerators, Spectrometers, Detectors and Associated Equipment*, vol. 952:161587, 2020. doi:10.1016/j.nima.2018.11.046.

[32] Overcast, W. C. Digital Aperture Photometry Utilizing Growth Curves. Master's thesis, University of Tennessee, 2010.

[33] Personal communication with A. Riffeser from the University Observatory of LMU Munich.

[34] Personal communication with operators of the ARCADE Raman LIDAR.

[35] Personal communication with operators of the FRAM telescope.

[36] Press, W. H., Teukolsky, S. A., Vetterling, W. T., and Flannery, B. P. Numerical Recipes (Cambridge University Press), 2007.

[37] Riello, M., et al. Gaia Early Data Release 3: Photometric content and validation. *Astronomy & Astrophysics*, 2020. doi:10.1051/0004-6361/202039587.

[38] Riffeser, A. Git repository with the growing curve program.
URL `https://github.com/arriusm/usmpy`

[39] Rista, J. Preliminary Analysis – ASI1600MM-Cool | Nature Photography (accessed on 02-12-2020).
URL `https://jonrista.com/the-astrophotographers-guide/the-zwo-asi1600-guide/the-zwo-asi1600/preliminary-analysis/`

[40] Romanishin, W. An Introduction to Astronomical Photometry Using CCDs (University of Oklahoma), 2002.

[41] Schulte, D. H. and Crawford, D. L. Tables for use at the Kitt Peak National Observatory. *Contributions from the Kitt Peak National Observatory, No. 10.*, 1961.

[42] Strasbourg astronomical Data Center (CDS). VizieR - Université de Strasbourg (accessed on 02-12-2020).
URL `https://vizier.u-strasbg.fr/viz-bin/VizieR`

[43] Wagner, R. M. Measurement of Very High Energy GammaRay Emission from Four Blazars Using the MAGIC Telescope and a Comparative Blazar Study. *Publications of the Astronomical Society of the Pacific*, vol. 119(860):1201–1203, 2007. doi:10.1086/522380.

[44] ZWO Company. ASI1600 Manual (accessed on 02-12-2020), 2018.
URL `https://astronomy-imaging-camera.com/`

Acknowledgements

I would like to thank my internal supervisor Prof. Dr. Thomas Kuhr from the LMU Munich and my external supervisor Jürgen Besenrieder from Max Planck Institute for Physics for the support they gave me during my Bachelor work. I am very grateful to work and learn in the MAGIC working group at MPP and want to thank Dr. Razmik Mirzoyan for giving me this great opportunity, for the valuable discussions we had and for his help in the review of the thesis.

Special thanks go to Dr. Arno Riffeser from the University Observatory of the LMU, who acted as an inofficial supervisor and whose advice, help and experience in the field of photometry were very helpful. I am especially grateful for his availability and support during the last two weeks of writing. On a similar note I need to thank Oliver Schütz from ESO, who has worked at the La Silla Observatory for many years. He explained basic and not so basic concepts of photometry to me and provided me with many valuable references.

I also want to thank all my colleagues in the MAGIC working group for their regular input, their readiness to answer my questions, their great willingness to help and some good ideas. Thanks to all of you who have reviewed and commented on this alarmingly long Bachelor thesis, and thanks to all who were available in the last weeks of the writing process, answering questions about LaTeX or other relevant topics.

Thanks to everyone else who also helped in the review, everyone who encouraged me with words or deeds and everyone who made my day better for example by playing music to me.

Last but certainly not least I have to thank my brother for always supporting me: Thank you!

Declaration

Hereby, I declare that I have composed the presented thesis independently on my own and without any other resources than the ones indicated.

Hiermit erkläre ich, die vorliegende Arbeit selbständig verfasst zu haben und keine anderen als die in der Arbeit angegebenen Quellen und Hilfsmittel benutzt zu haben.

Munich, December 16, 2020

Marine Pihet